International Journal of Solids and Structures 322 (2025) 113598

Contents lists available at ScienceDirect

International Journal of Solids and Structures

journal homepage: www.elsevier.com/locate/ijsolstr

Image-based modelling of open cell polymeric foams as simplified beam structures

Shaoheng Feng [a,*], Luca Andena [a], Michele Nacucchi [b], Fabio De Pascalis [b]

[a] *Dipartimento di Chimica, Materiali e Ingegneria chimica “Giulio Natta”, Politecnico di Milano, Piazza Leonardo da Vinci, 32, 20133 Milano, Italy*
[b] *ENEA, Division for Sustainable Materials, Research center of Brindisi, Cittadella della Ricerca, SS7 km 706, 72100 Brindisi, Italy*

ARTICLE INFO

Keywords:
Polymeric foams
X-ray computed tomography
Beam element model
Mechanical properties

ABSTRACT

Polymeric foams have many important applications in various industrial sectors, thanks to an excellent combination of properties. The study of the mechanical behavior of this type of material has important academic value and application prospects but poses important challenges because of their complex topology; numerical models faithful to their geometrical microstructure suffer from very high computational costs. This paper aims to develop a simplified beam element model of open-cell polymer foams based on X-ray computed tomography (CT) images, able to describe their compressive response with significantly improved computational efficiency. The images of the microstructure of a PPI20 polyurethane foam were obtained through CT scan. These images were then converted to 3D solid model, from which key morphological features were extracted. Based on these morphological features, an equivalent simplified beam element model was generated. A good quantitative agreement was found between simulations carried out with the two numerical models (solid and beam) and the compression experiments. In-situ compression tests performed in combination with CT scans also confirmed the ability of numerical models to describe the real deformation mechanisms of the foam. This simplified model demonstrates an accuracy comparable to the 3D solid model with vastly reduced computational effort, allowing for an efficient and accurate prediction of the mechanical properties of open cell foams.

1. Introduction

Due to the serious energy crisis in human society, the need for lightweight materials has become increasingly important in daily lives. Open cell polymeric foams can be regarded as a composite material with polymer as the matrix and gas as a co-continuous phase structure. The driving force behind their invention and development has been the reduction of the material density combined with an adequate performance, thereby achieving the purpose of lightweighting. Open cell polymeric foams have attracted much attention in different industries due to their advantages such as light weight, high specific strength, heat / sound insulation and low price. This type of material has been widely used in the fields of automobile and aviation industry, renewable energy, shock absorption, packaging, construction industry, gas storage and separation materials and even catalysis (Jacobs et al., 2008; Amir et al., 2018; de Souza et al., 2022). In actual applications, different fields have different requirements for the microstructure of foam materials.

Real morphological features of the foams are often aperiodic, inhomogeneous, and disordered (Matzke, 1945; Matzke, 1946; Kraynik et al., 2003; Kraynik, 2003; Kraynik et al., 2004); an extensive and accurate experimental characterization of these materials is challenging and could be affected by undesired variations induced during sample preparation. Moreover, it is very difficult to predict the effects generated by even small variations in the foam morphology, reducing the ability to transfer data obtained on a given foam sample to a different foam product. To address these issues, theoretical research and numerical computational methods have been widely exploited to study the mechanical properties and microstructure evolution of polymeric foams.

Matzke (Matzke, 1945) determined the structure of 1,000 bubbles in a soap foam by optical observations, which provides important cell structure information for related research. He also observed 600 liquid bubbles under a microscope and found that the number of cell faces per cell ranged from 11 to 17, with an average of 13.7 (Matzke, 1946). Given this variability, sophisticated statistical models are needed to obtain more accurate predictions. In the early stage of theoretical research on foam materials, the theory of slender beams was mainly used to analyze and characterize foam properties (Gent and Thomas, 1959; Lederman, 1971). Then, based on the idealized unit cell, many analytical or

---

* Corresponding author.
E-mail address: shaoheng.feng@polimi.it (S. Feng).

https://doi.org/10.1016/j.ijsolstr.2025.113598
Received 7 February 2025; Received in revised form 6 August 2025; Accepted 8 August 2025
Available online 11 August 2025

experimental models have been developed to predict the mechanical properties of foams. For three dimensional (3D) foams, cubes, tetrahedrons, dodecahedrons, and tetrakaidecahedrons are used as repeating cells. A crossed cube model for open cell foams was proposed by Gibson and Ashby (Gibson and Ashby, 1982). Recent unit cell-based models, which able to derive structure–property relationships, were developed by employing tetrakaidecahedrons (Zhu et al., 1997; Warren and Kraynik, 1997; Li et al., 2003).

The microstructure of a typical open-cell foam consists of struts that form a network of interconnected polyhedron-like cells. At the pore-scale analysis level, the characteristic cellular structure inside an open cell foam can be modeled employing different methods:

(1) The basic shape characteristics of the struts, and the distribution characteristics of the skeleton network, can be described in a simplified manner by approximating them as a polyhedral network structure; this assumption is motivated since the microstructure of open cell foams is governed by the principle of minimum surface energy (Kraynik, 2003) acting during bubble foaming. The advantage of this foam structure reconstruction model is that the scale parameters of the stacked cells and the approximate spatial organization structure are considered; these variables reflect the shape characteristics of each strut realistically, and in some cases the constructed three-dimensional structure is similar to the internal structure of the real foam; valid analytical solutions can be derived for most models. This type of reconstructed structure has been widely used, and many complete and effective foam material structures and finite element models have been developed, including the cubic cell model (Warren and Kraynik, 1988; Ghosh, 2009; Klumpp et al., 2014), Weaire–Phelan model (Buffel et al., 2014), Kelvin cell model (Mills, 2007; Jang et al., 2008; Jang et al., 2010; Kaoua et al., 2016), Voronoi model (Song et al., 2010; Martínez et al., 2017; Wang et al., 2020) and other polyhedral structure models (Li et al., 2003; Inayat et al., 2011), as shown in Fig. 1. While the simplified model geometry can be a good approximation of a single cell, the main disadvantage of this approach lies in the loss of information about the actual geometrical variability within the foam cell population.

(2) The three-dimensional structure of the foam can be captured and reconstructed using advanced imaging methods such as X-ray computed tomography (CT) or Scanning electron microscopy (SEM), although the latter is mostly limited to 2D reconstruction. Compared with the first method, the detailed morphology of the foam is preserved, including the real shape of the struts and the true distribution of dimensions within the skeleton network. A model based on this reconstructed structure can fully simulate the interactions between the struts under deformation. In recent years, such reconstruction models have been increasingly used in the structural analysis and compression deformation research of foams (De Jaeger et al., 2011; Ramírez et al., 2014; Tagliabue et al., 2021; Belda et al., 2021). The reconstruction of detailed structures has a positive impact on the accurate prediction of the mechanical properties of foams. Therefore, relevant experiments and simulations including quasi-static compression tests (Daphalapurkar et al., 2008), strain-rate effect (Sun et al., 2016; Bhagavathula et al., 2022) and anisotropy (Jang et al., 2009; Singh et al., 2010) of foams have been considered by researchers using X-ray tomography. There is a strong endeavor to relate these mechanical properties to the explicit morphology of foams. The

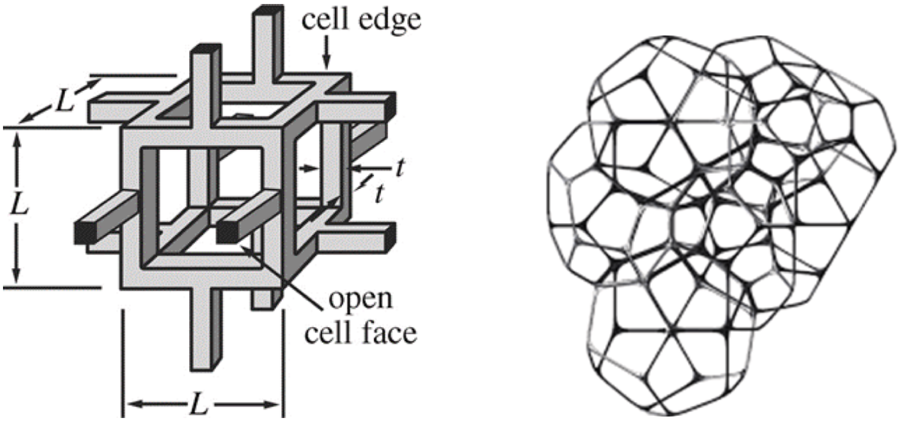

(a) Cubic cell model

(b) Weaire–Phelan model

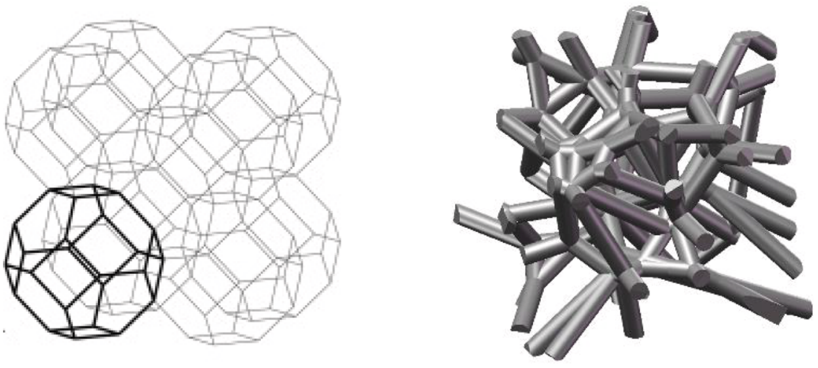

(c) Kelvin cell model

(d) Voronoi model

Fig. 1. Examples of different models for open cell foams.

observations acquired using X-ray tomography have shown that this technique is suitable for studying the relationship between 3D structure and deformation of polymeric foams (Elliott et al., 2002; Adrien et al., 2007).

The finite element models established by the above methods are mostly 3D solid element models. As the geometric complexity of the foam cell topology increases, the number of calculations required for accurate modeling and analysis using 3D solid elements become challenging. The design of the foam structure requires repeated iterations and hundreds of structural mechanical performance analyses, making the optimization of the structure extremely difficult and inefficient, a fact which also limits the large-scale application of this method to real engineering problems. Very fine structures, as in the case of high-porosity foams with relatively small strut diameters, require fine 3D solid meshes and are particularly expensive to model, since the computational time increases exponentially with the decrease of the mesh size.

A possible solution lies in the use of beam elements for modeling; this approach is commonly used for analyzing the mechanical properties of lattice structures and open cell foams (Gong et al., 2005; Gaitanaros et al., 2012; Tran and Niiranen, 2020; Liu et al., 2021; Weeger et al., 2023; Zhou et al, 2024). Although the replacement of solid elements with beam elements greatly improves calculation efficiency while preserving the overall structure, this method has certain limitations. The results predicted by 3D solid elements are consistent with the experimental results in most strut diameter-to-length ratio ranges, while a beam element model is usually not able to accurately reproduce the stiffness of the structure: the conversion neglects the strut joint area, which can be regarded as an agglomeration of strut ends (as shown in Fig. 2). The differences between the results obtained with beam element models and experimental data can be attributed to the uniform cross-section of the beam model, while the joint region where more struts converge is typically thicker. To compensate for this limitation, inherent in a pure beam model, several methods have been proposed. Luxner el al. (Luxner et al., 2005) artificially increased the Young's modulus of the material assigned at the ends of beam elements by 1000 times. Große et al. (Große et al., 2008) used the Weaire-Phelan model which is based on the assumptions of spherical joints and joint-strut overlap. Labeas and Sunaric (Labeas and Sunaric, 2010) considered two end portions, measuring each 1/10 of the total cylindrical beam length, and increased locally the radius by 40 %. Smith et al. (Smith et al., 2013) also adopted the same method to increase the stiffness of the beam element models. Gaitanaros et al (Gaitanaros et al., 2012) considered the uneven distribution of the strut cross section area, defining a beam element based on the correlation between the cross-section area and strut length. The density of the foam was subsequently used to correct the problem of overlapping material at the vertex. With these corrections, simulations based on beam elements can recover good accuracy and may represent the ideal strategy for simulating and analyzing lattice structures. However, these arbitrary modifications do not take into account the actual microstructural characteristics of the foam.

In the present study, a simplified finite element model of open-cell foam based on beam elements was established. This model extracts the microstructural parameters of the foam, retains its detailed morphological features, and reduces the total degrees of freedom and number of elements of the model, greatly improving the efficiency of numerical calculations. This simplified beam model takes into account the increased stiffness at the joint area of struts, by means of variable cross-section beam elements whose geometrical features remain linked to the real foam morphological parameters.

2. Definition of variable cross-section beam element

A uniform cross-section beam element model can replace each strut in the foam with a beam which has the same length L and thickness T of the strut. The nodes are subjected to loads such as axial force, shear force and bending moment, resulting in combined axial tension, compression and bending deformation. Each strut is treated as an element for finite element analysis, which has two nodes. Each node has six DOFs, as shown in Fig. 3.

The displacement U and force F of each node can be expressed by the following matrix:

$$U = \left[u\, v\, w\, \theta_x\, \theta_y\, \theta_z \right]$$

$$F = \left[P\, V\, W\, \varphi_x\, \varphi_y\, \varphi_z \right] \tag{2.1}$$

Under the premise of linear elasticity and small deformations, there is a linear relationship between the nodal forces and the nodal displacements when the element is in equilibrium, shown in Eq. (2.2):

$$F = KU \tag{2.2}$$

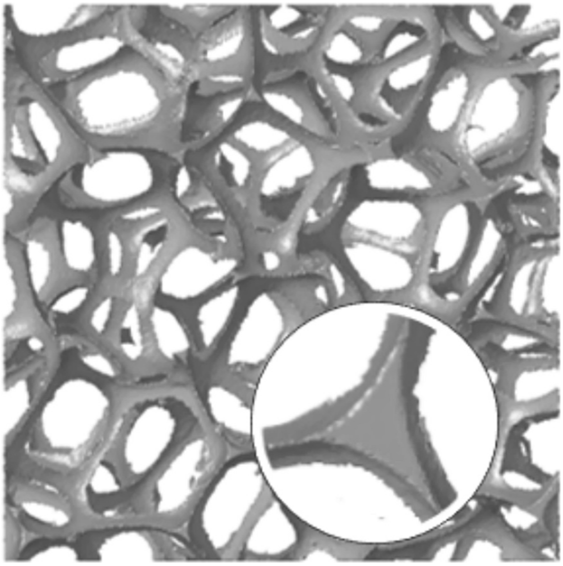

Fig. 2. Struts joint area.

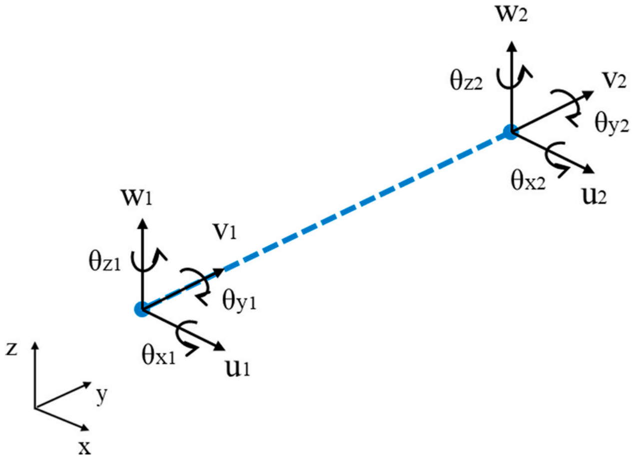

Fig. 3. Sketch of a 2-node beam element with its related degrees of freedom.

In the formula, K is the stiffness matrix. It can be divided into four parts (K^1, K^2, K^3 and K^4) to simplify its expression:

$$\left[\begin{array}{cccccc|cccccc}
\frac{12\Phi_z EI_z}{L^3} & 0 & 0 & 0 & 0 & -\frac{6\Phi_z EI_z}{L^2} & -\frac{12\Phi_z EI_z}{L^3} & 0 & 0 & 0 & 0 & -\frac{6\Phi_z EI_z}{L^2} \\
0 & \frac{AE}{L} & 0 & 0 & 0 & 0 & 0 & -\frac{AE}{L} & 0 & 0 & 0 & 0 \\
0 & 0 & \frac{12\Phi_x EI_x}{L^3} & \frac{6\Phi_x EI_x}{L^2} & 0 & 0 & 0 & 0 & -\frac{12\Phi_x EI_x}{L^3} & \frac{6\Phi_x EI_x}{L^2} & 0 & 0 \\
0 & 0 & \frac{6\Phi_x EI_x}{L^2} & \frac{EI_x(3\Phi_x+1)}{L} & 0 & 0 & 0 & 0 & -\frac{6\Phi_x EI_x}{L^2} & \frac{2\Phi_x EI_x}{L} & 0 & 0 \\
0 & 0 & 0 & 0 & \frac{GJ}{L} & 0 & 0 & 0 & 0 & 0 & -\frac{GJ}{L} & 0 \\
-\frac{6\Phi_z EI_z}{L^2} & 0 & 0 & 0 & 0 & \frac{12\Phi_z EI_z}{L^3} & \frac{6\Phi_z EI_z}{L^2} & 0 & 0 & 0 & 0 & \frac{2\Phi_z EI_z}{L} \\
\hline
-\frac{12\Phi_z EI_z}{L^3} & 0 & 0 & 0 & 0 & \frac{6\Phi_z EI_z}{L^2} & \frac{EI_z(3\Phi_z+1)}{L} & 0 & 0 & 0 & 0 & \frac{6\Phi_z EI_z}{L^2} \\
0 & -\frac{AE}{L} & 0 & 0 & 0 & 0 & 0 & \frac{AE}{L} & 0 & 0 & 0 & 0 \\
0 & 0 & -\frac{12\Phi_x EI_x}{L^3} & -\frac{6\Phi_x EI_x}{L^2} & 0 & 0 & 0 & 0 & \frac{12\Phi_x EI_x}{L^3} & -\frac{6\Phi_x EI_x}{L^2} & 0 & 0 \\
0 & 0 & \frac{6\Phi_x EI_x}{L^2} & \frac{2\Phi_x EI_x}{L} & 0 & 0 & 0 & 0 & -\frac{6\Phi_x EI_x}{L^2} & \frac{EI_x(3\Phi_x+1)}{L} & 0 & 0 \\
0 & 0 & 0 & 0 & -\frac{GJ}{L} & 0 & 0 & 0 & 0 & 0 & \frac{GJ}{L} & 0 \\
-\frac{6\Phi_z EI_z}{L^2} & 0 & 0 & 0 & 0 & \frac{2\Phi_z EI_z}{L} & \frac{6\Phi_z EI_z}{L^2} & 0 & 0 & 0 & 0 & \frac{EI_z(3\Phi_z+1)}{L}
\end{array}\right] = \begin{bmatrix} K^1 & K^2 \\ K^3 & K^4 \end{bmatrix} \tag{2.3}$$

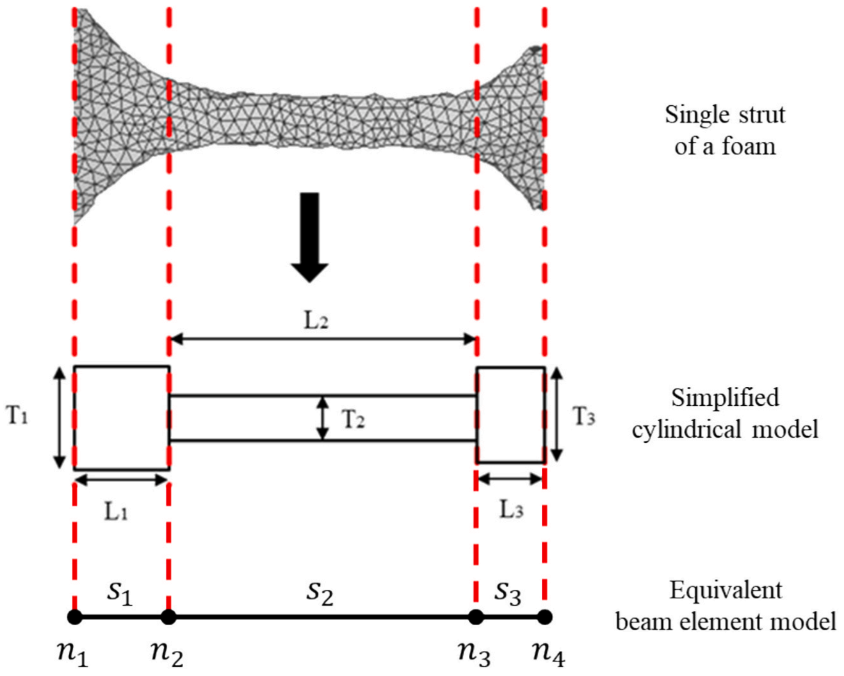

Fig. 4. Variable cross-section beam element for a single strut.

The parameters that affect the stiffness of the strut are the length L, the cross-section area A of the beam element, the Young's modulus E and shear modulus G of the constituent material, the polar moment of area J, the shear correction factor K_s, and the second moments of area I_x and I_z. The parameter $\Phi_{(x,z)}$, which is a function of these variables, also appears in Eq. (2.4):

$$\Phi_x = \frac{1}{1+\frac{12EI_x}{AGK_sL^2}}, \Phi_z = \frac{1}{1+\frac{12EI_z}{AGK_sL^2}} \tag{2.4}$$

To account for the influence of the joint area of the struts on the structural stiffness, a variable cross-section beam element model is proposed. In this paper, the shape of each strut is considered to be a cylinder, and the cross section of the strut at any given position is approximated by a circle. Thus, the thickness of the strut at this position is the diameter of its corresponding cross section. The variable cross-section beam element model is constructed based on the uniform cross-section beam element and is modified into a combination of three uniform cross-section beams with lengths of L_1, L_2, and L_3 and thicknesses of T_1, T_2, and T_3 respectively, as shown in Fig. 4.

When the material and cross-sectional profile are the same, the mathematical expression of the stiffness matrix of the uniform cross-section beam element can be defined as a function of L and A. In this study, the cross section of the beam is regarded as circle, so section area A can be represented by the thickness T. Then the stiffness of each section can be expressed according to Eq. (2.5):

$$K = f(L, T) \tag{2.5}$$

Finally, the global stiffness matrix of the variable cross-section beam can be defined as:

$$K_v = \sum_{i=1}^{3} K_i = \sum_{i=1}^{3} f_i(L_i, T_i) \tag{2.6}$$

Fig. 4 shows that a variable cross-section beam element includes three segments (S_1, S_2 and S_3) and four nodes (n_1, n_2, n_3 and n_4). The segments at the two ends represent the joint areas of the struts in the foam, while the middle segment represents the non-intersecting part of the strut. K_1, K_2 and K_3 are their relevant stiffness matrixes. Therefore, the combined stiffness matrix K_v of the variable cross-section beam element can be written as:

$$K_v = \begin{bmatrix} K_1^1 & K_1^2 & 0 & 0 \\ K_1^3 & K_1^4 + K_2^1 & K_2^2 & 0 \\ 0 & K_2^3 & K_2^4 + K_3^1 & K_3^2 \\ 0 & 0 & K_3^3 & K_3^4 \end{bmatrix} \tag{2.7}$$

The final stiffness matrix of the foam can then be determined by the combination of the stiffness matrix of each strut. In order to calculate the combined stiffness matrix of each strut, the length and the thickness of different parts of the variable cross-section beam need to be measured. The images of the foam microstructure obtained from CT (computed tomography) scan were used to achieve the measurement of these morphological parameters.

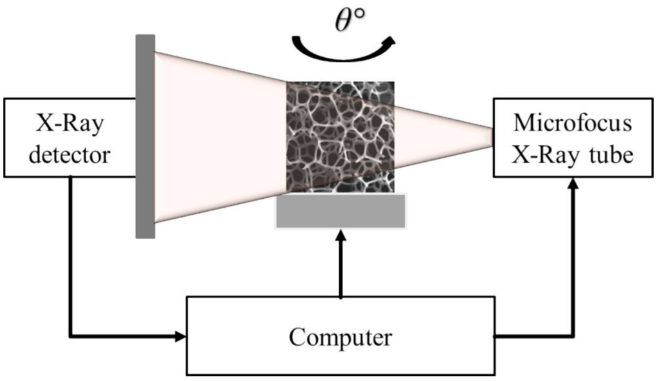

Fig. 5. Microstructure of foam scanned by X-ray computed tomography (CT).

3. Morphological feature characterization

Open cell foams are composed by a large number of polyhedral cells, resulting in a network of interconnected pores. The edges around the pores are called struts or ligaments, which connect the nodes to form a solid matrix enclosing the entire porous domain. To indicate the type of foam, manufacturers typically calculate the number of pores per linear inch (PPI), combined with porosity and/or relative density. Porosity alone is not sufficient to quantify foam structure; pore shape and size and strut characteristics (length, thickness and cross-section shape) should be specified in addition.

In recent years, computed tomography (CT) has been widely used in the study of polymeric foam microstructure (Elmoutaouakkil et al., 2003; Adrien et al., 2007; Pérez-Tamarit et al., 2018). This technology can intuitively and non-destructively display the microstructure of the material layer by layer in grayscale images. These images can be further converted to a three-dimensional microstructure model of the material, which can restore the cell morphology and topological structure characteristics of the foam material to the finest detail, with accuracy that other methods cannot match.

The PU open cell foam used in this study was produced by Yuanshengxing Electronic Materials Co., Ltd, China. in the form of sheets of dimensions 400 x 300 x 20 mm with a nominal density of 40 kg/m^3 ± 10 % and a relative density 2.7 % ± 0.25 %. This material is mainly installed inside electronic components to exploit its good shock absorption, filtering and flame retardation properties. No information about the formulation or production parameters was available. To characterize the morphological features of the foam, the images of the microstructure of PU PPI20 with the dimension of 10 mm x 10 mm x 10 mm were obtained using x-ray CT, as shown in Fig. 5. The CT scanning was performed using a GE Phoenix Nanotom CT system equipped with a 180 kV /15 W nano focus X-Ray tube and a 12-bit 2300 x 2300-pixel Hamamatsu flat panel detector. All analyses were performed with a molybdenum target suitable for weakly absorbing samples, such as the foams investigated in this work. The acceleration voltage and beam current of the X-ray tube were set to 50 kV and 180 μA, respectively. The isotropic voxel size for each sample was set to 8 μm. The volume reconstruction was performed using the application Phoenix datos|x 2. This software is able to convert a series of X-ray projections acquired while rotating the sample 360° into a resulting slice stack representing the actual digital volume reconstruction through a filtered back-projection algorithm.

In order to effectively and accurately measure the microstructural characteristics of the foam, the images obtained by CT scanning need to be processed first. The image treatment process is shown in Fig. 6. The images of the foam structure obtained from CT scan are grayscale images. Each image contains two different phases: pores and struts. These images were first processed by applying a median filter (Kirchner and Fridrich, 2010) to reduce the noise and were then binarized and segmented using the level-set method (Li et al., 2010). Then, the binary images were used to determine the morphological features of the microstructure of the foam. All the operations were conducted with user-defined scripts written in MATLAB.

3.1. Strut length measurement

To measure the length of foam struts, a 3D model of the foam microstructure was generated from the images using the aforementioned level set method (Teran et al., 2005; Li et al., 2021) and Delaunay triangulation (Rebay, 1993). An Erosion Thickness (ET) skeletonization algorithm (Yan et al., 2016) was then applied on the model to extract

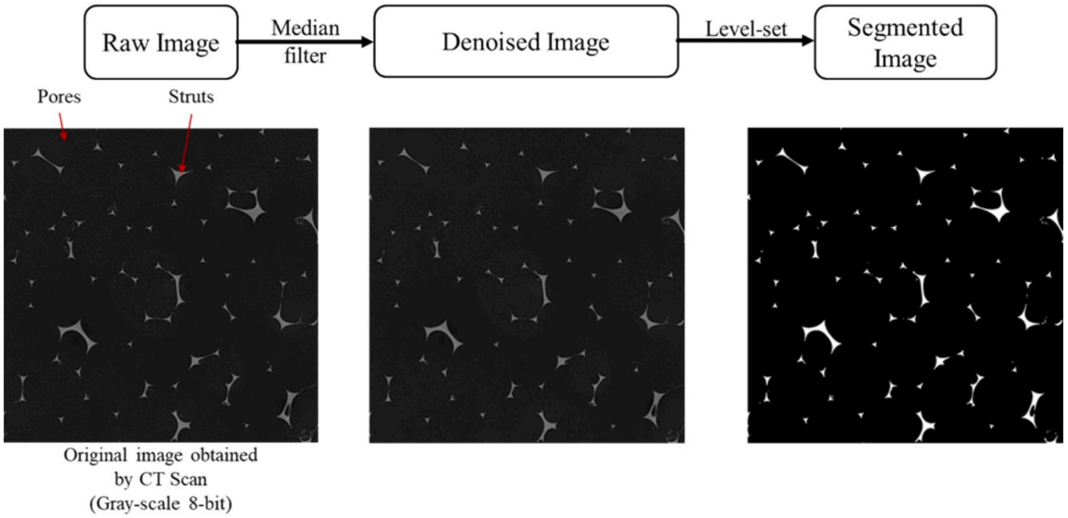

Fig. 6. Image treatment procedures.

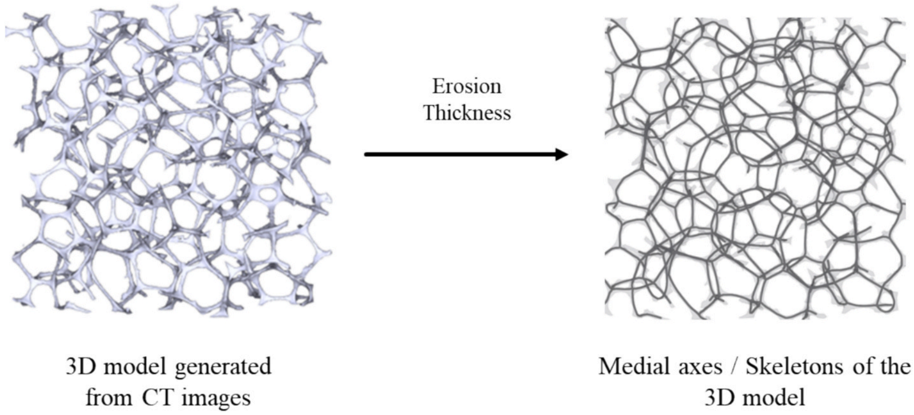

Fig. 7. Medial axis extraction using Erosion Thickness.

medial axis / skeletons of the structure. ET can produce skeletons that are stable under boundary perturbations, which helps to capture clean, shape-revealing and topology-preserving skeletons from 3D models. Fig. 7 shows the extraction of medial axis from a PPI20 foam cell.

The final medial axis contains three types of nodes. In image processing, pixel connectivity refers to the relationship between a pixel/voxel in a two/three-dimensional image (or hypervoxels in n-dimensional images) and its neighboring pixels. 26-connectivity was used to find the neighbor points of a node in skeletons in 3D space. The nodes with only 1 neighbor are called end nodes (see the blue hollow circles in Fig. 8). The nodes with more than 2 neighbors are vertices (black hollow circles in Fig. 8). The nodes with exactly 2 neighbors are the nodes on simple struts. Based on this, the whole connected medial axes were separated into isolated struts and labeled. Then the distance between two end points of a separated strut was measured as the length. Two kinds of length were considered: the curve length Lc – which coincides with the physical length of a strut; and the chord length Le, which is the Euclidean distance between two end points (shown in Fig. 9).

Fig. 10 reports the histogram showing the distribution of strut lengths for the PPI20 foam sample. The average Lc and Le are 1.169 mm and 1.062 mm respectively.

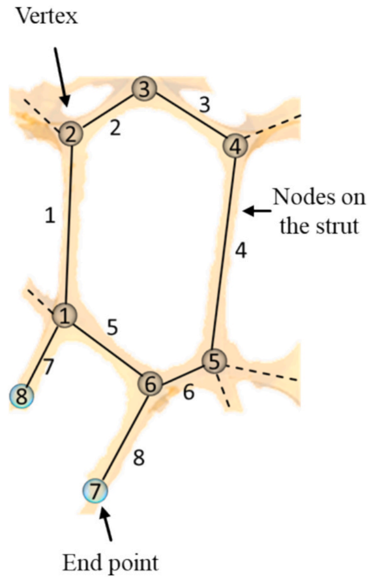

Fig. 8. Node classification in foam structure.

3.2. Strut thickness measurement

In image analysis, the Euclidean distance map (EDM) assigns to each pixel/voxel of the binary image the distance to the nearest obstacle

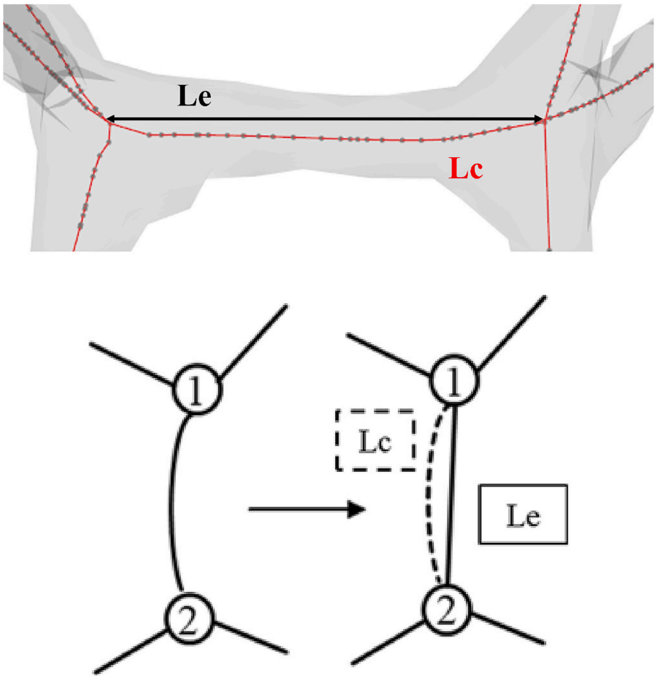

Fig. 9. Determination of strut curve and chord length (*Lc* and *Le*, respectively).

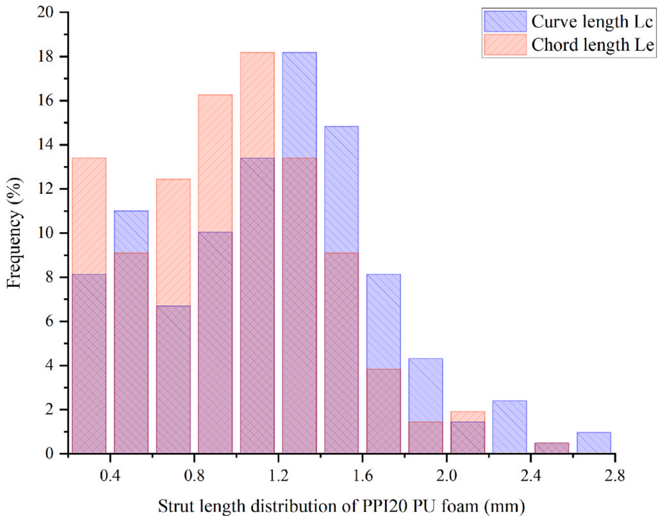

Fig. 10. Strut length distribution of PPI20 foam.

(Danielsson, 1980). That is, the value of each pixel/voxel is the distance to the nearest background pixel/voxel (for background pixels/voxels, the EDM is 0).

To measure the thickness of the struts, the distance transform was applied to obtain the EDM on a 3D binary image of the foam. For the convenience of explanation, a 2D demonstration of the thickness calculation is illustrated in Fig. 11, where the binary image of five connected struts is shown; the value of white pixels is 1, representing strut material, while the 0 value is assigned to black pixels denoted to pores. Fig. 11(b) shows the EDM after distance transform of the binary image. The intensity value inside the strut pixel expresses the distance to the nearest pore pixel. After the skeletonization using the algorithm ET mentioned in section 3.1, the medial axes of struts were extracted according to the procedure detailed below (Fig. 11(c)), then separation and labeling were applied to obtain the labeled isolated medial axis (Fig. 11(d)).

The thickness of each strut can be calculated using Eq. (3.1):

$$T = 2 \bullet I \bullet R \tag{3.1}$$

where I represents the intensity value in the EDM along the medial axis, i.e. the skeleton, and R represents the resolution of the image. In this way, the thickness along the length of the strut can be determined.

Fig. 12 shows the histogram with the distribution of strut thickness measurements for the PPI20 foam sample. The average strut thickness is 0.114 mm.

The measurements of the length and thickness of each strut are the basis to develop the variable cross-section beam element approach illustrated in section 4.

It is known that the cross-section area of the strut also varies along the strut medial axis. In the work of Gong et al., 2005 and Jang et al., 2008, the axial variation of the struts cross section of polyurethane foams was characterized with a symmetric four-order function, improving the agreement with experimental data. Based on these studies, De Jaeger et al. (De Jaeger et al., 2011) developed a comprehensive model to account for the variations in strut cross-sectional shape and diameter using the Heywood roundness factor and a fourth-order polynomial expression, respectively. A model that includes the actual shape of the struts was proposed by Kumar and Topin (Kumar and Topin, 2014; Kumar et al., 2015). The two studies propose strut geometric shapes such as circles, squares, diamonds, hexagons, and stars, without considering the actual strut shapes of open cell foams with a specific porosity. To verify the accuracy of the distance map method applied in this study and to study the variation of the strut cross section along the strut length, the strut profile function was introduced. The strut profile, S, is used to describe the cross-sectional size and morphology along the length of each strut (shown in Fig. 13) where O is the middle point of the strut, L is the strut length and t_m is the thickness in the middle of the strut.

The strut profile at a given location along l is denoted as $S(l)$. This is determined by the intersecting line profiles between the cross-sectional planes and the strut surface at any given location. The foam strut cross sections are similar to the Plateau border geometry (Plateau, 1873). Zhu et al. (Zhu et al., 1997) also observed Plateau border geometries in the cross-sections of struts in foam cells. The cross-section of the strut in open cell foams is then often characterized by a three-cusp hypocycloid shape known as Plateau border (Gong et al., 2005; Jang et al., 2008; Jang et al., 2010), in this study, the cross-section of the struts was instead approximated as circular. Consistently, the strut thickness along the strut length was determined by finding the diameter of an equivalent circle with the same area of the intersecting profile. Here, the local strut thickness profile S_{ij} was fitted with a second-order polynomial:

$$S_{ij}(l) = \left(1 + al/L + b(l/L)^2\right)t_m \tag{3.2}$$

where a and b are parameters to fit. To study the general morphology characteristics of all struts, each individual strut profile with its own length and thickness was normalized (shown in Fig. 14(a)). The average strut profile ($S(l) = (1 - 0.187l/L + 1.918(l/L)^2)t_m$) was also fitted (see Fig. 14(b)).

The comparison of strut thickness measured by the two methods is shown in Fig. 15. Little difference was found between the two distributions. The distance map was chosen to measure the strut thickness in this study because of its higher calculation efficiency.

3.3. Material density determination

Relative density is a key factor in determining the strength and other properties of foams. In some modelling methods of open cell foams, to correctly represent the material distribution in the actual foam, the excess material at nodes was removed by cutting the ends of beams. The amount of removed material depends on the relative density (See Gong et al., 2005; Jang et al., 2008). In order to accurately determine the

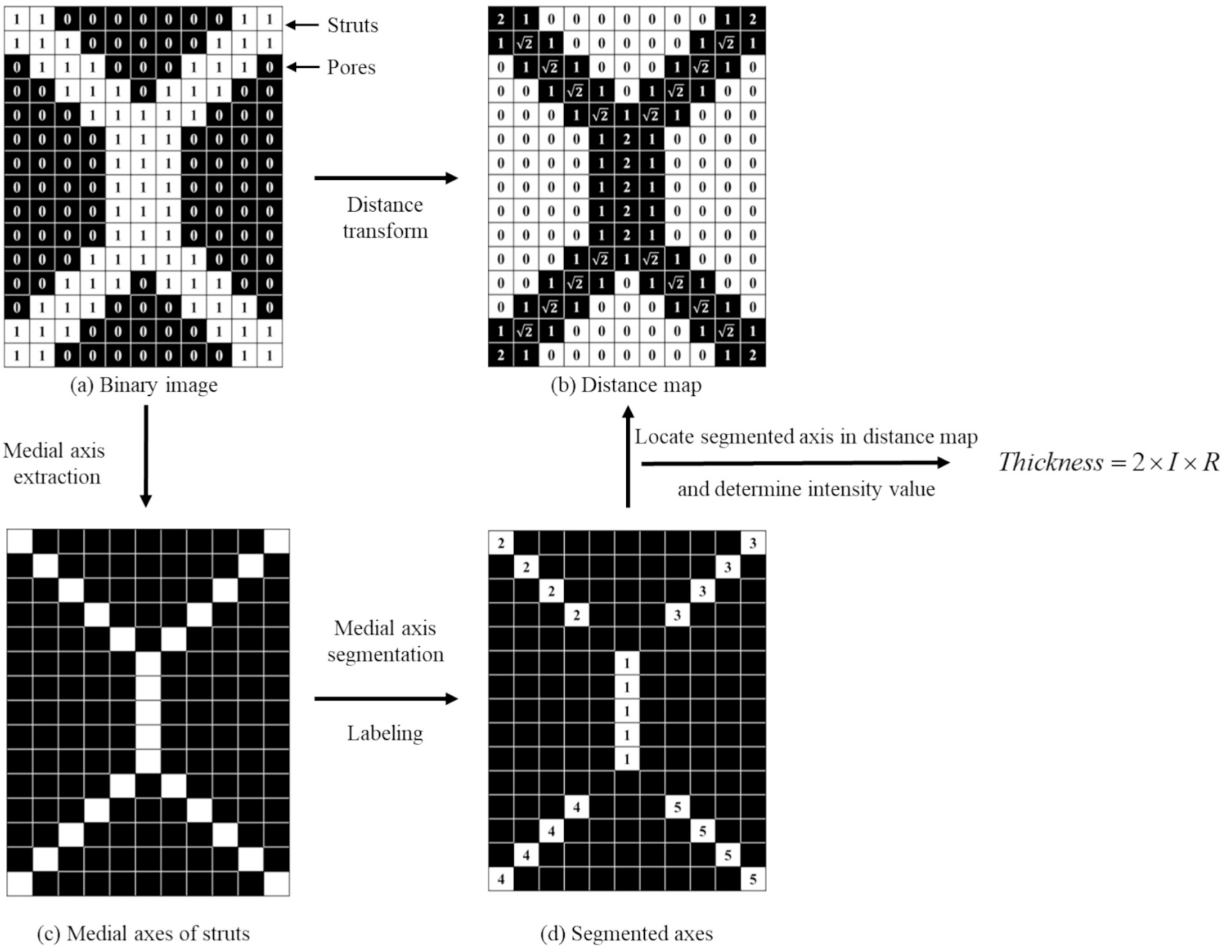

1	1	0	0	0	0	0	0	0	1	1
1	1	1	0	0	0	0	0	1	1	1
0	1	1	1	0	0	0	1	1	1	0
0	0	1	1	1	0	1	1	1	0	0
0	0	0	1	1	1	1	1	0	0	0
0	0	0	0	1	1	1	0	0	0	0
0	0	0	0	1	1	1	0	0	0	0
0	0	0	0	1	1	1	0	0	0	0
0	0	0	0	1	1	1	0	0	0	0
0	0	0	0	1	1	1	0	0	0	0
0	0	0	1	1	1	1	1	0	0	0
0	0	1	1	1	0	1	1	1	0	0
0	1	1	1	0	0	0	1	1	1	0
1	1	1	0	0	0	0	0	1	1	1
1	1	0	0	0	0	0	0	0	1	1

(a) Binary image

2	1	0	0	0	0	0	0	0	1	2
1	$\sqrt{2}$	1	0	0	0	0	0	1	$\sqrt{2}$	1
0	1	$\sqrt{2}$	1	0	0	0	1	$\sqrt{2}$	1	0
0	0	1	$\sqrt{2}$	1	0	1	$\sqrt{2}$	1	0	0
0	0	0	1	$\sqrt{2}$	1	$\sqrt{2}$	1	0	0	0
0	0	0	0	1	2	1	0	0	0	0
0	0	0	0	1	2	1	0	0	0	0
0	0	0	0	1	2	1	0	0	0	0
0	0	0	0	1	2	1	0	0	0	0
0	0	0	0	1	2	1	0	0	0	0
0	0	0	1	$\sqrt{2}$	1	$\sqrt{2}$	1	0	0	0
0	0	1	$\sqrt{2}$	1	0	1	$\sqrt{2}$	1	0	0
0	1	$\sqrt{2}$	1	0	0	0	1	$\sqrt{2}$	1	0
1	$\sqrt{2}$	1	0	0	0	0	0	1	$\sqrt{2}$	1
2	1	0	0	0	0	0	0	0	1	2

(b) Distance map

(c) Medial axes of struts

2										3
	2								3	
		2						3		
			2				3			
					1					
					1					
					1					
					1					
					1					
			4				5			
		4						5		
	4								5	
4										5

(d) Segmented axes

Fig. 11. 2D demonstration of the application of EDM to measure the strut thickness.

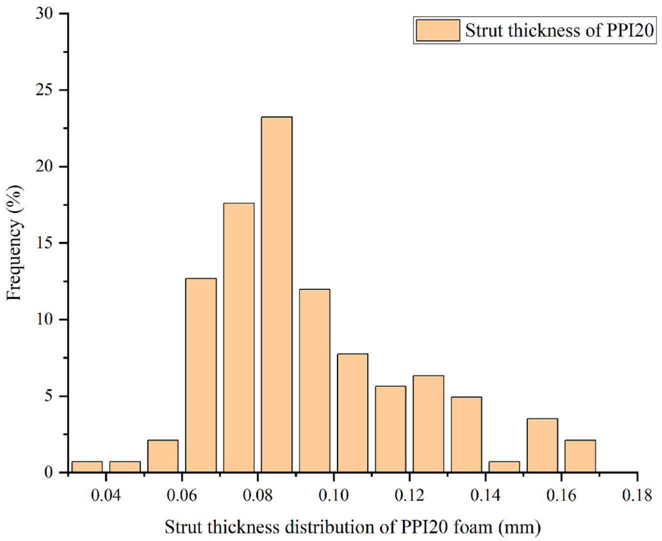

Fig. 12. Strut thickness distribution of PPI20 PU foam.

relative density of the open cell foam reconstructed model, the binarized images of the microstructure were used. The relative density ρ_r of the foam is the ratio of the foam density ρ_f to the density of the constituent material ρ_m. In essence, it represents the percentage of a given volume occupied by the foam structure, shown in Eq. (3.3).

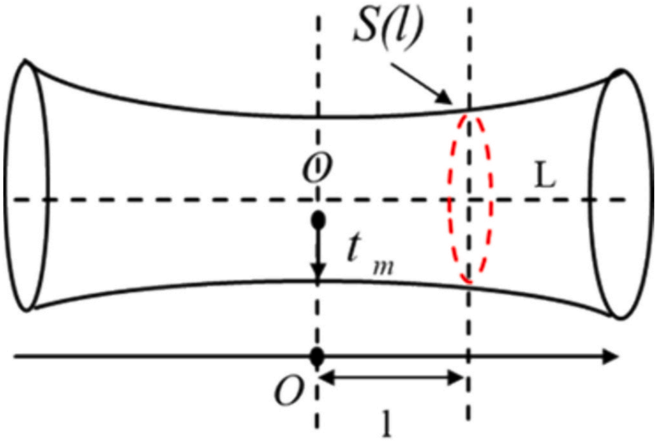

Fig. 13. Strut profile S along the strut length.

$$\rho_r = \rho_f / \rho_m = V_m / V_f \tag{3.3}$$

where V_m represents the volume occupied by the solid material and V_f is the total volume of the foam sample.

Using Matlab, a 3D stack of binary images was processed. Then the total number of voxels N_{total} was calculated, representing the total volume of the foam sample. The number of voxels N_f with the intensity value equal to 1 was also counted, which is the volume occupied by the struts. Then, the relative density can be immediately obtained through

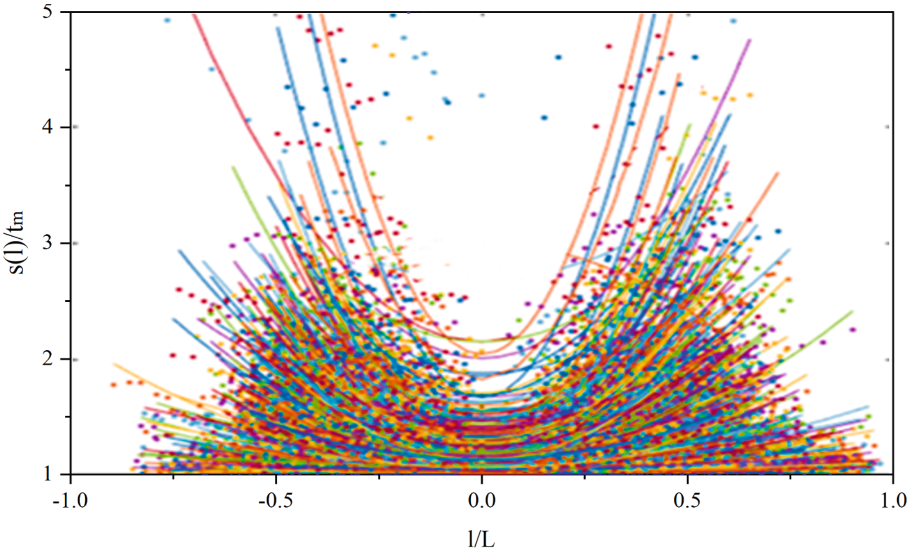

(a) Strut profile for all analyzed struts

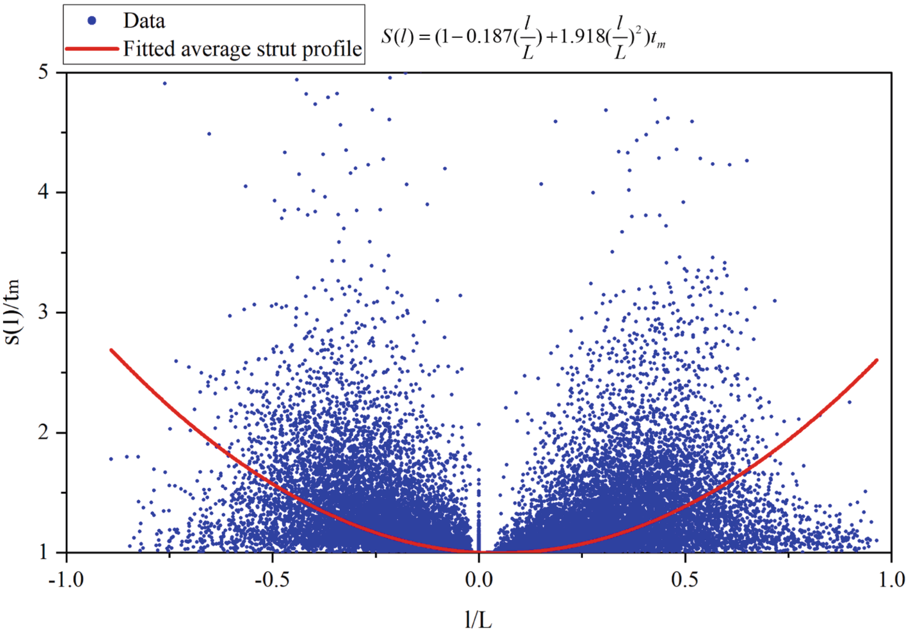

(b) Average strut profile

Fig. 14. Strut profiles of PPI20 foam.

the ratio of N_f over N_{total}. In this study, the relative density calculated from the image was 2.66 %, a value which is consistent with the data provided by the supplier. This result has the same order of magnitude as the relative density value reported in Gong et al., 2005. The difference may be caused by the different production methods and materials.

To perform the simulation, the absolute density of the constituent material PU is also required; it was measured with a Pycnomatic ATC Thermo Scientific gas pycnometer following the ASTM D6226–21, 2021 standard. Five cubic specimens were used; they were cut randomly along the sheet to increase the statistical validity of the results. Measurements were conducted in pure helium atmosphere (Helium 5.0, purity grade) at 23 °C and at an equilibrium pressure of 200 kPa. The PU density measured by this method is 1.45 ± 0.065 g/cm^3. An evaluation performed assuming the nominal and relative densities provided by the supplier gives 1.48 g/cm^3, which is very close to the value determined experimentally.

3.4. Pore size distribution and structural anisotropy

Conventional PU foams often display an anisotropic cell structure, with their properties varying depending on the direction with respect to the foaming one (also referred to as the rise direction, see Gong et al., 2005). The structure of a single pore typical of PPI20 foam is shown in Fig. 16(a). The directions in this study are set as follows: the foaming

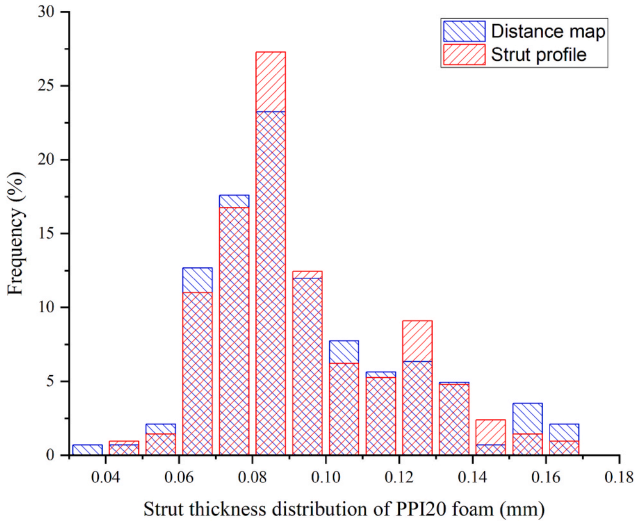

Fig. 15. Comparison between the strut thickness measured by different methods.

direction is noted as the Z-axis and the other two orthogonal directions are denoted as the X- and Y-axis.

In this study, image processing methods were used to characterize the pore size distribution and structural anisotropy. Pore segmentation (shown in Fig. 16(b)) was determined using the watershed algorithm (Shafarenko et al., 1997). The volume is the product of the total number of voxels occupied by each pore times the image resolution constant, R^3. The pore size distribution of PPI20 PU foam is shown in Fig. 16(c). The average pore size is 13.73 mm^3.

To measure the structural anisotropy of the foam, the classical Mean Intercept Length (MIL) method (Harrigan et al., 1984) was used. A set of parallel lines along a large number of different directions (ω) in the 3D binary image were superimposed on the binary object with volume V. The number of intersections with the phase interfaces I(ω) along any of these lines was then counted. MIL as a function of ω can finally be computed as:

$$\mathrm{MIL}(\omega) = h/I(\omega) \tag{3.4}$$

where h is the summation of the length of all traced lines. The MIL in different directions can be shown in a rose plot (Fig. 17), and the 3D diagram can be fitted with an ellipsoid whose parameters define a second-order tensor (Harrigan et al., 1984). This tensor is symmetric, and its eigenvalues and eigenvectors decomposition provide insights about the predominant object orientations. The data can also be processed using covariance calculations to define an orientation matrix from which the fabric tensor is derived (Ketcham et al., 2004; Tagliabue et al., 2021). With this approach, the degree of anisotropy (DA) can be calculated as the ratio of the largest to the smallest eigenvalue ($\lambda_{\max}$ and $\lambda_{\min}$). The calculation gave a degree of anisotropy for this PU PPI20 foam

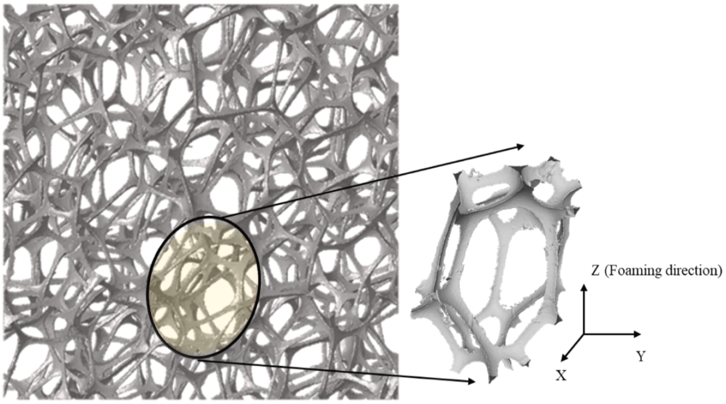

(a) Foam structure and direction regulations

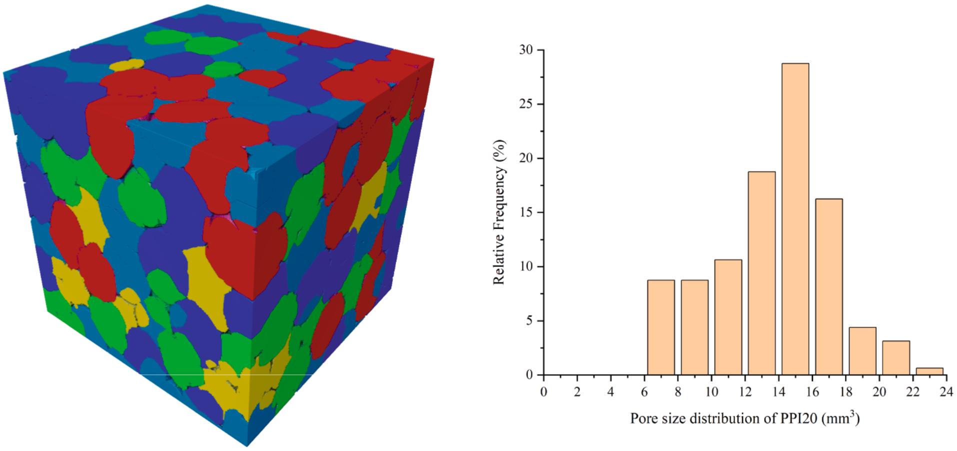

(b) Pore segmentation (c) Pore size distribution

Fig. 16. Pore size distribution of PPI20 PU foam.

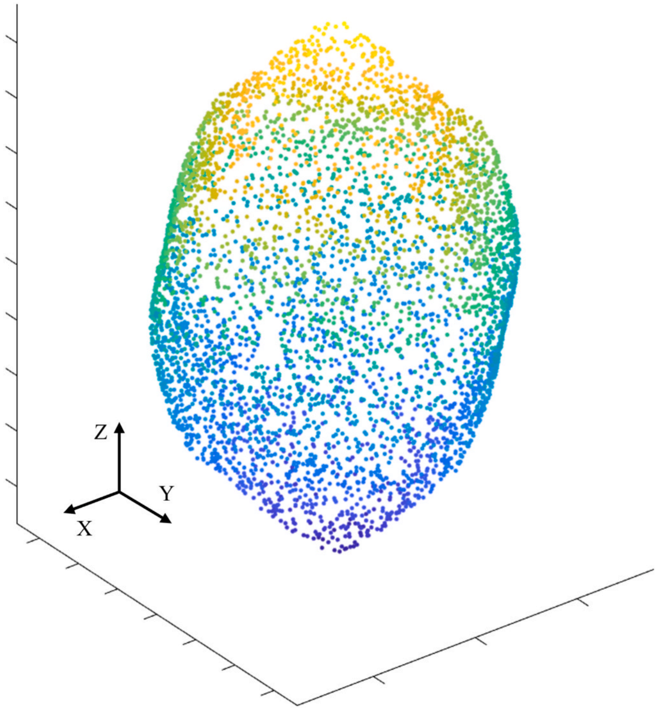

Fig. 17. Mean intercept length point cloud of PPI20 foam.

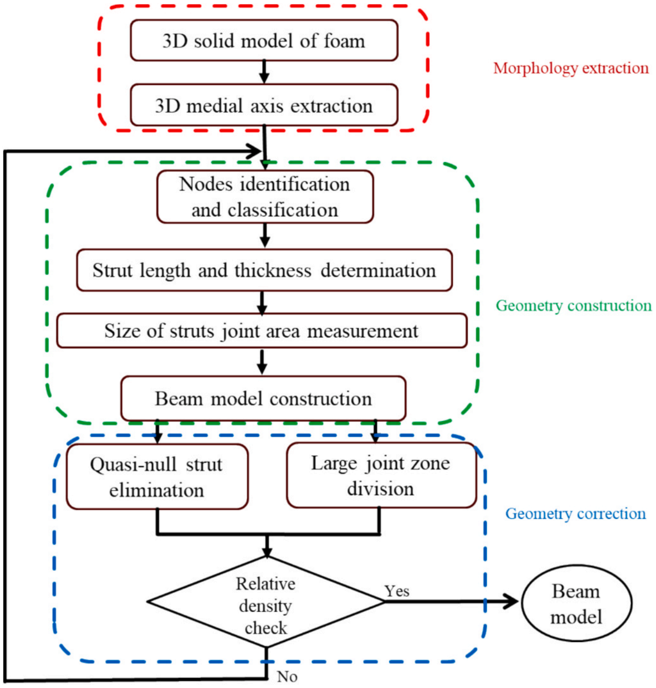

Fig. 18. Workflow to generate variable cross-section beam model.

equal to 1.63.

4. Variable cross-section beam model generation

Due to the complex structure of polymeric open cell foams, the number of solid elements in a model constructed from CT images would be extremely large to guarantee an adequate description of the actual strut geometry, resulting in a significant increase in computational efforts. In this study, the open cell foam structure was considered as an assembly of rod-like struts which could be regarded as constant cross-section beams; a beam element model can thus be used to simulate the mechanical properties of the foam and simplify the calculations. However, a model based on uniform cross section beam elements would neglect the morphological characteristics of the strut joint area, compromising the accuracy of numerical calculations. To make up for this shortcoming, some studies proposed user-defined beam elements to replace the single strut of periodic lattice structures and consider the effect of the joints (Dong and Zhao, 2018; Park and Rosen, 2018). These methods are hardly applicable to model open cell polymeric foams with complex microstructures, because in the process of constructing user-defined elements, different types of simulations (such as tension, compression, bending, etc.) need to be performed on a single strut to obtain the equivalent stiffness matrix parameters, which is extremely costly for open cell foams with hundreds or thousands of struts with different morphologies. In this study we adopted a different strategy. Based on the standard Timoshenko beam element available in Abaqus, an improved beam element model of the PU PPI20 open cell foam is proposed considering the different morphological features of different struts.

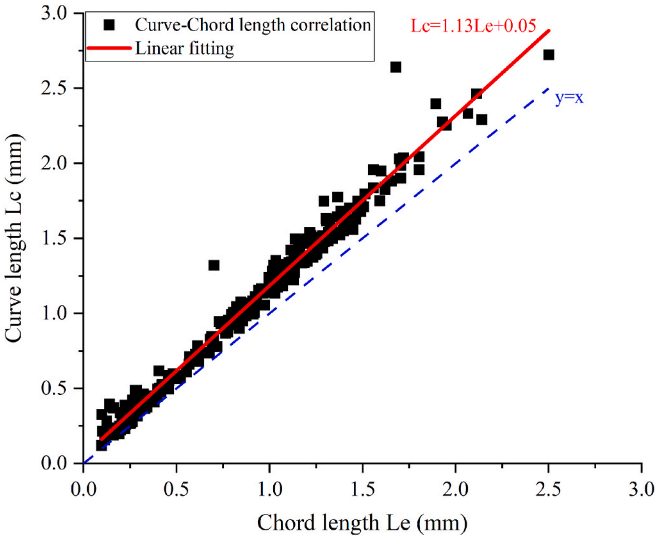

Fig. 19. The correlation between curve length *Lc* and chord length *Le*.

To incorporate the joint area of the struts in the beam model, each strut is considered as a combination of three parts. To construct the variable cross-section beam element, 6 geometrical parameters are needed, i.e. the length and thickness of the three segments of the strut. The workflow to generate the variable cross-section beam model is shown in Fig. 18, with its three main phases highlighted in different colors.

(1) Morphological feature extraction

The CT images of the foam were converted to a 3D solid model using Level-set method and Delaunay triangulation. The ET algorithm was then applied on the model to extract the medial axes of the structure.

(2) Geometry construction

− Strut length measurement

The different types of nodes were identified, and the individual struts labeled. The curve length *Lc* and the chord length *Le* were measured. The ratio R_L between *Lc* and *Le* was calculated. For the PPI20 foam sample, a linear correlation was found as shown in Fig. 19. The average R_L of the foam is 1.13, which indicates that the curvature of the strut is small. Consequently, it is reasonable to choose the chord length as the length of the beam elements to facilitate the measurement and improve the efficiency.

After the measurement of the total length of each strut, the length of the end segments was first determined. The geometrical parameters of

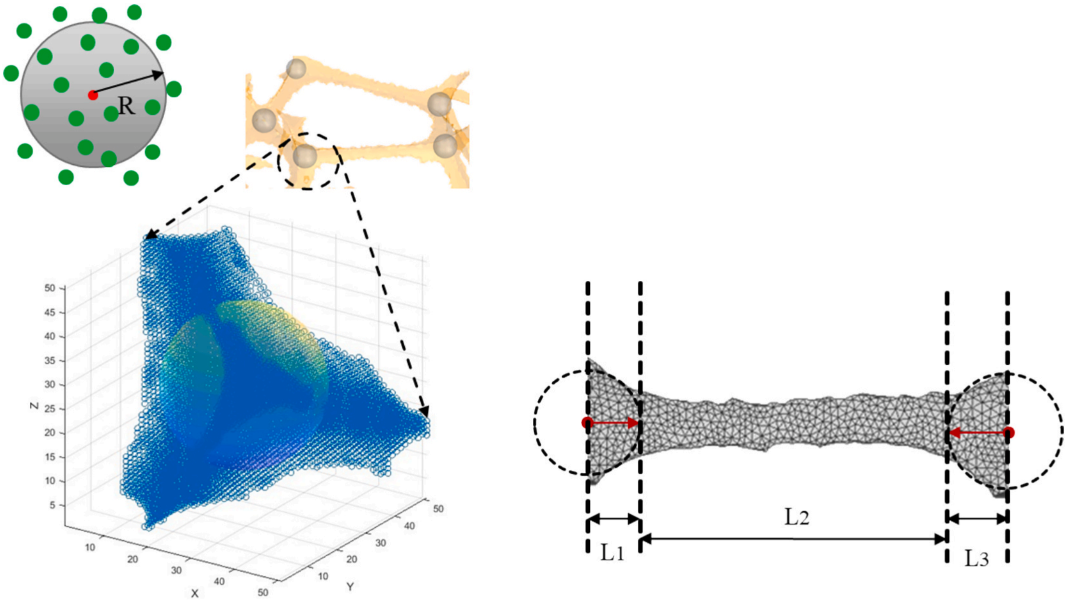

Fig. 20. The length determination of the three segments of the cross-section beam.

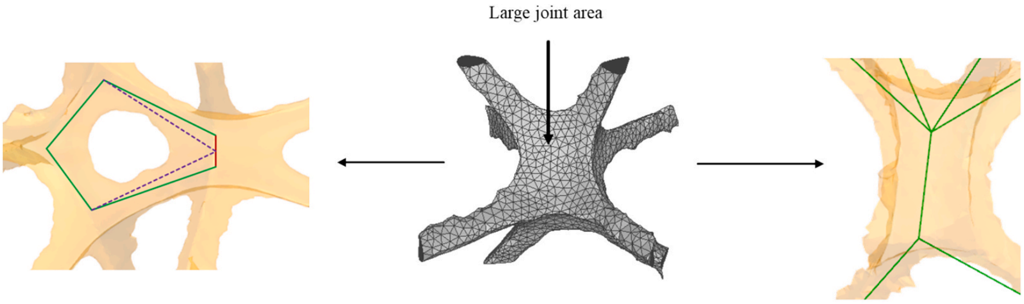

(a) Short strut elimination

(b) Preservation of long strut

Fig. 21. Geometry correction of joint area medial axis extraction.

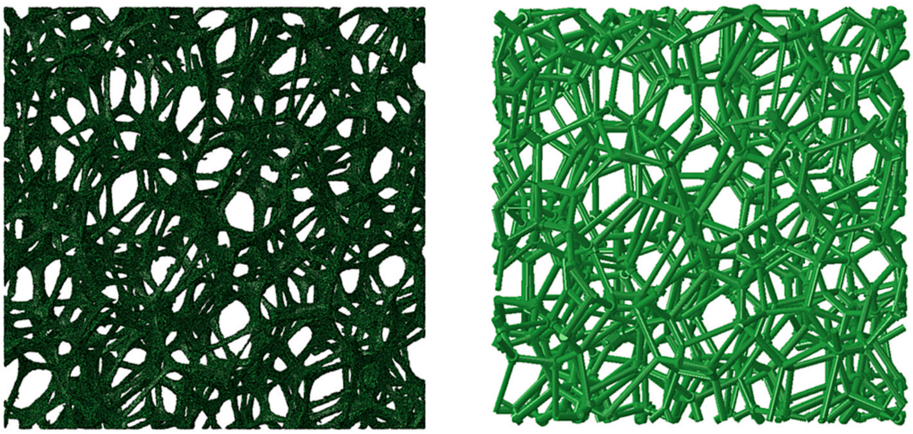

Solid model

Beam model

Fig. 22. Comparison between solid model and beam model.

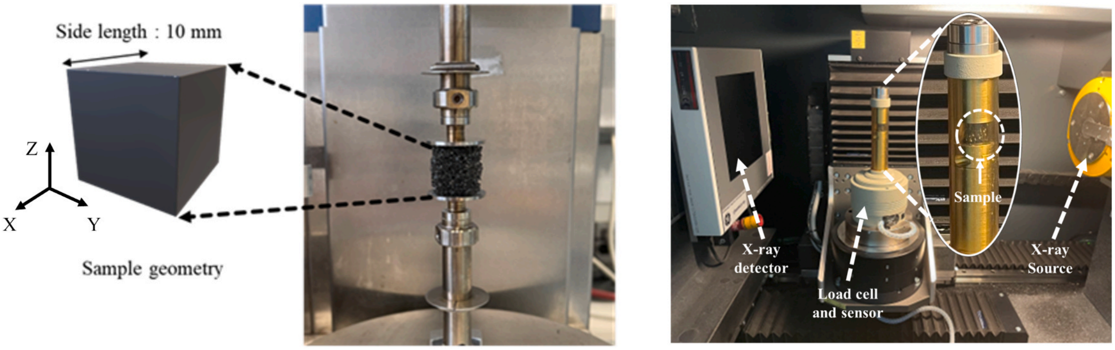

Fig. 23. Compression tests using RSAIII (left) and In-situ compression tests in CT machine (right).

these two segments define the joint area region. Each joint was replaced by a sphere whose radius corresponds to the length of the longer concurring beam end segment. An example of a joint area at the convergence of multiple struts is shown in Fig. 20. The length of the middle beam is the remaining length of the original beam, once the two end segments have been isolated.

– Strut thickness calculation

EDM was calculated from the CT images. The thickness of each strut was measured. The cross section of the struts is considered to be circular in this study, and uniform along the length of each beam segment (based on the results discussed in section 3.2); the radius of the cross section is taken as half the average beam thickness.

(3) Geometry correction

The microstructure of open-cell foams is complex and irregular. During the foaming process, it is difficult to ensure uniform distribution of the matrix material in the struts. This results in different sizes of strut joints. Generally, ET will not generate a medial axis in the joint area but only generate the intersection points of several medial axes. However, when more than four struts intersect in the joint area, the size of this area increases, and the medial axis would be extracted. When the length of the medial axis of this zone lied below a given tolerance the central point of the medial axis was retained and connected to adjacent nodes to eliminate this artificially generated strut (as shown in Fig. 21(a)). When the medial axis was longer, it was preserved instead (see Fig. 21(b)). In this study, the tolerance value was set to 0.1 mm, which guarantees that the length change of the connected strut would not exceed 10 % of its original length.

(4) Beam model construction and primary verification

The variable cross-section beam elements were connected to form the final beam model. The comparison between beam model and solid model is shown in Fig. 22. The relative densities of the beam model and solid model are 2.6 % and 2.7 %, respectively. The two values are very close, and this result supports the reliability of this image-based reduced order model generation method. The generated models were then imported in ABAQUS to perform the compression simulations, as discussed in the next section 5.

5. Materials and experiments

5.1. Compression tests on PU foam samples

In this study, quasi-static compression tests were performed on PPI20 foam samples using two different setups: a RSAIII dynamic testing machine and an in-situ compression test fixture positioned inside the CT scanner (Deben Microtest system), as shown in Fig. 23. While tests conducted on the RSAIII generally gave more accurate results, the in-situ setup allowed the study of the deformation evolution of the foam microstructure during the compression process. The specimens used for compression tests were cut from foam sheets using hot wire. The same dimension of the cubic samples was used for the two testing methods, equal to 10 mm x 10 mm x 10 mm (also shown in Fig. 23). The compression tests were performed along the foaming direction – Z axis. All the compression tests were carried out at room temperature (23 ± 1°C). On the RSAIII machine, 30 compression specimens were tested. Due to the complexity and time of the CT scan operation, only 3 samples were tested in-situ. In all cases, samples were tested up to 50 % nominal strain by applying a constant displacement rate of 1 mm/min, corresponding to a nominal strain rate of $1.67e^{-3}$ s^{-1}, according to the standard ASTM D1621–16, 2023; the loading rate level is similar to that applied in Gong et al., 2005. Preliminary testing at different rates (up to 6 mm/min) suggested almost negligible rate effects in this range, consistently with the rubbery nature of the polymer which at room temperature is well above its glass transition. The force–displacement response for each test was recorded on both setups, and the nominal

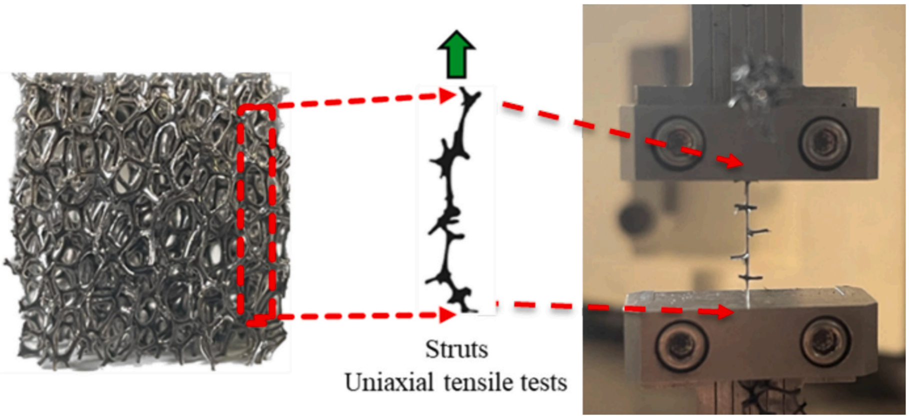

Fig. 24. Quasi-static tensile test performed on the struts.

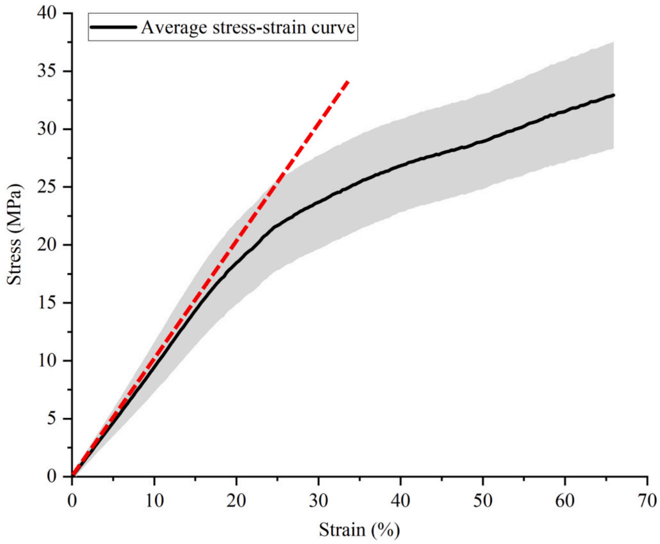

Fig. 25. Average stress strain curve of isolated struts.

stress–strain curves were derived. In addition, to characterize the mechanical anisotropy of the material, the compression tests were also performed along the other two transverse directions (Y axis and X axis) using the RSAIII machine. The loading conditions (loading rate, temperature) are the same as the compression tests along the Z axis.

For the in-situ tests, CT scans of the samples were acquired (according to the procedure illustrated in section 3) at the beginning and at the end of the test. For the second scan at 50 % strain, an interval of 5 min was introduced between stopping the test and the CT acquisition, to allow complete relaxation of the samples still under compression. The 3D models at initial 0 % strain and final 50 % strain were generated using the images acquired at these two deformation stages; the model at 0 % strain was taken as the basis to perform the numerical calculations.

5.2. Characterization on the constituent material of the PU foam

To perform the simulation, the mechanical properties of the constituent material, PU, need to be determined. To obtain a direct measurement, consistent with the conditions of the material after the foaming process, several isolated struts with a total length of about 25 mm were cut from the foam sheet. These struts were considered to have a constant circular cross section obtained by calculating the average diameter value measured along the length of the strut, measured using an optical microscope. Then, quasi-static uniaxial tensile tests (shown in Fig. 24) were carried out on the RSAIII machine at 3 mm/min to characterize the mechanical properties of this constituent polyurethane. 20 samples were tested and the average stress–strain curve is shown in Fig. 25. The shaded error bar area corresponding to the standard deviation of the measured values was also plotted. The deformation was completely recovered after the test, thanks to the elastomeric behaviour of the PU foam.

In this study, different constitutive equations were considered (including linear elastic, elasto-plastic and hyperelastic) to describe the mechanical behavior of the constituent PU material. Although the compressive response of PU foam could possibly be influenced by the loading rate (See Gong et al., 2005), preliminary testing on the elastomeric PU used in this research indicated that rate-effects are quite small, and consequently the present model does not include any visco-elastic component. Using the stress strain curve, the constitutive parameters of solid PU used in simulation can be calculated through curve fitting. Taking the calculation of Young's modulus of the material as an example, performed according to the standard ASTM D638-14, 2022, a red dotted straight line in Fig. 20 was drawn as an extrapolation of the initial linear portion of the stress–strain curve; the Young's modulus can then be obtained by the slope of this line. The comparison of the simulations conducted with the solid foam model using different constitutive laws and experimental parameters is shown in the Appendix. A high degree of consistency between the different material models and the experimental results was reported. This may sound surprising at first, given the markedly nonlinear behavior reported in Fig. 25; however, the deviation from linearity is relatively limited and only a tiny fraction of the struts reaches strain levels higher than 20 %. Additionally, hyperelasticity is not available with beam elements in Abaqus/Explicit. Given the substantial equivalence of the different options, the simpler linear elastic law was chosen in view of improving the calculation efficiency, with identified parameters reported in Table 1. The value of the Poisson's ratio of PU was taken from the literature, after verifying that choosing different values gave almost no effect within the range 0.30–0.45 (see Appendix). To reproduce the real test conditions, the steel compression platens were also introduced in the model. The elastic properties used for steel are also shown in Table 1.

Table 1
Mechanical properties of steel and PU.

Materials	Young's modulus E	Poisson's ratio υ	Density
steel	210 GPa	0.3	7.85 g/cm^3
PU	93 MPa	0.4	1.45 g/cm^3

Table 2
Mesh information for different models.

Model	Mesh type	Number of elements	Number of Nodes
Beam model	B32	8472	16,559
Solid model	C3D4	1,467,243	436,893

6. Simulations

Compression of the PPI20 foam was simulated using both the beam and solid models with ABAQUS / Explicit. The whole cubic sample tested was modelled. The material constitutive parameters are input using the parameters obtained in section 5.2. The mesh setting is a critical step that determines the accuracy of the simulation results. In this study, the Timoshenko beam element was chosen. To obtain accurate numerical calculation results, a fine mesh is required. Initially, each strut is composed of three beam elements. Each beam element is then refined, and the total number of elements is increased. A mesh sensitivity analysis was conducted to determine the optimal element size; results are shown in the Appendix.

Relevant mesh information including mesh size, element type and element numbers is shown in Table 2. The analysis step is set to "General", "Dynamic, Explicit". After several analyses and tests, an appropriate mass scaling value was selected to accelerate the simulation process of the solid model: for the elements whose stable time increment was less than $5\cdot10^{-8}$ the latter was increased to $1\cdot10^{-7}$. In Abaqus/Explicit, 'contact' generates contact forces to resist node-into-face, node-into-analytical rigid surface, and edge-to-edge contact penetration across the all-inclusive surface, thereby providing a comprehensive solution for enforcing contact in a wide range of simulation scenarios without the need for complex contact definition procedures. The definition of an appropriate method to model arbitrary contact between beam elements remains an open problem. One approach to modeling beam contact is to introduce a spring contact model into the unit cell (Gong and Kyriakides, 2005). In this study, 'General contact (All with self)' was enforced to model contact between platens and the sample and also mutual contact between the polymeric struts. The tangential behavior in the contact properties was set to penalty, based on previous experiences on polymeric foam modelling; the friction coefficient was set to a fixed value of 0.2, after verifying that any values within the

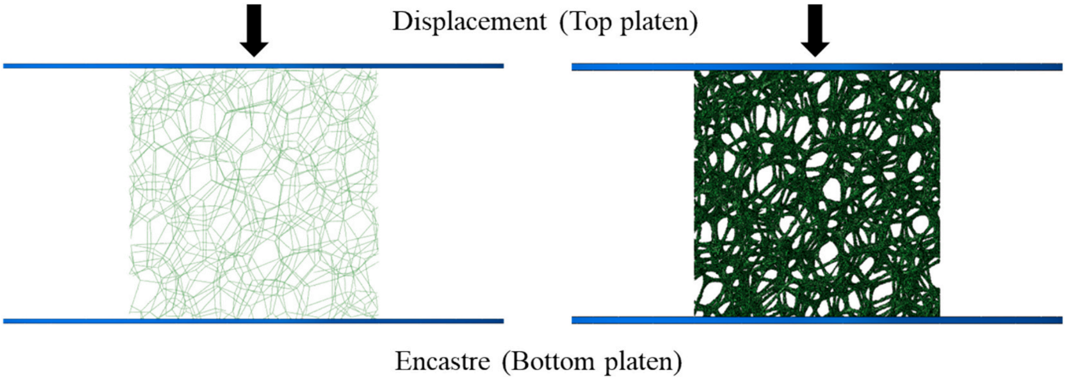

Fig. 26. Boundary conditions applied in simulation for beam (left) and solid (right) model.

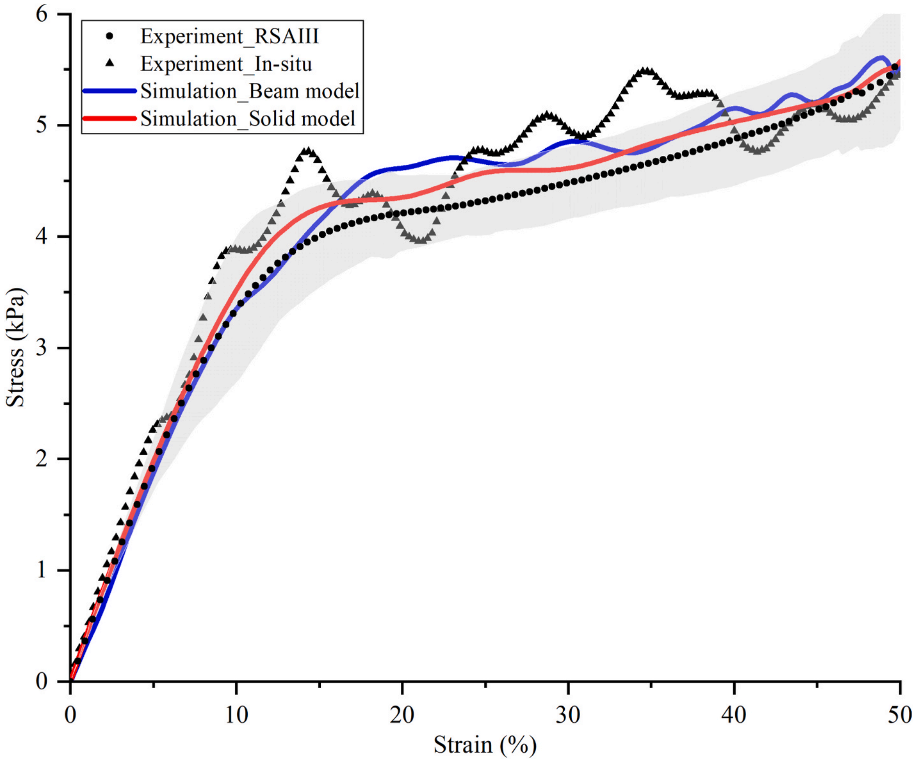

Fig. 27. Stress–strain curves for compression tests and simulations.

range 0.1–0.3 gave little or no effect on the outcome of the simulations (shown in the Appendix). The normal behavior was instead set to “hard” contact. A rigid body constraint was applied to the two platens. During the simulation the lower platen position is fixed. In the compression step, a downward displacement was applied on the upper platen while horizontal displacement was kept fixed. The boundary conditions applied on the foam during compression are shown in Fig. 26.

7. Results and Discussion

7.1. Stress–strain behavior

The comparison between the stress–strain curves of simulations using different models and experimental results along foaming direction (Z-axis) are shown in Fig. 27.

The symbols represent the experimental results obtained on the two different setups (RSAII and in-situ). The shaded area around the RSAIII dataset represents the deviation for 30 tests. A single in-situ experimental result was chosen due to the fact that both solid and beam models were generated using the images obtained through this in-situ compression test. At the early stage of compression, the foam shows a linear elastic behavior. This is followed by a plateau region at the strain level beyond 10 % of relatively constant force with increasing deformation. The specific details of these states and the transitions between them are highly dependent on the foam microstructure (Zhu and Windle, 2002; Kraynik, 2003; Gong et al., 2005). As the displacement of the platen increases further, the volume of the densified structure gradually increases, and the resistance to the platen becomes greater. Load oscillations occurred, especially during the in-situ tests. During the compression, due to the sparse foam structure, the contact area between the specimen and the platen constantly changes, and deformations of internal structures such as collapse also cause instability. The experimental data obtained using RSAIII, however, are much smoother than the in-situ experimental data. The RSAIII is a dedicated and very accurate testing device, and the related dataset is also larger. Conversely, the accuracy of the in-situ testing apparatus is lower and the degree of

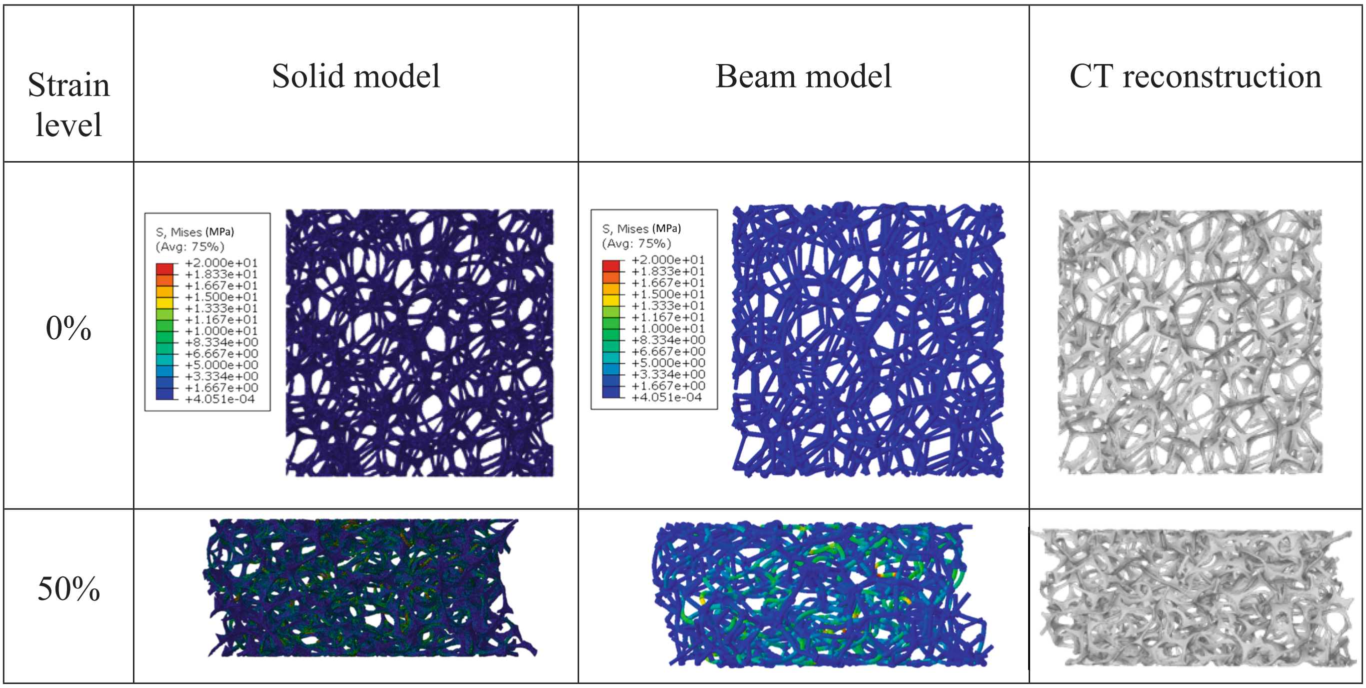

Fig. 28. Contour map of Von Mises stress (in MPa) for the two numerical models, compared against the experimental CT reconstruction at 0% and 50% compressive strain.

control over sample loading not as good; the origin of the relatively large oscillations reported is not fully clear. Nevertheless, the in-situ platform allows the CT scanning of foam samples during compression, and in the end the results provided are certainly comparable with the reference curves provided by the RSAIII (in principle they should return the same compressive behaviour of the foam). It is worth remarking that deformations are completely recovered after the test, with no residual strain or damage visible in the elastomeric foam samples.

The red and blue solid lines represent the outcome of the numerical simulations performed using the solid and beam model, respectively. The solid model results show very good agreement with the experimental results, with only a slight overestimation of the plateau stress level. The results of the beam model are very similar. Irrespective of these minor differences, the behavior predicted by the beam element model still provides an accurate description of the experimentally observed one, with a similar overestimation of the plateau stress. This slight loss of accuracy comes with the advantage of a huge reduction in the computational effort, as demonstrated later.

The stress–strain curves along different directions are shown in the Appendix. The Young's modulus of X-, Y- and Z-axis are 41 kPa, 24 kPa and 20 kPa respectively. The initial modulus of the two transverse responses is approximately half that of the foaming direction. Considering the other loading directions, this PU foam was shown to be transversely isotropic from stress-strain curves obtained through both experiments and simulations. The material has similar compression behavior in the X- and Y-axis. The compressive behavior along the foaming direction is stiffer than that along the other two directions. This result is consistent with the conclusions obtained in Kanakkanatt, 1973, Huber and Gibson, 1988 and Gong et al., 2005. The simulation results using the solid element model and the beam element model show a good correlation to the experimental results. These two CT image-based finite element analysis methods can effectively capture the transversely isotropic nature of this material.

Table 3
Comparison between computational cost of beam and solid model.

Model	Number of elements	CPU time (s)	Memory allocation (GB)
Beam model	8472	14469	0.46
Solid model	1467243	276967	6.60

7.2. *Deformation analysis*

The 3D foam microstructure at 0 % strain level and 50 % strain level is shown in Fig. 28 for the images obtained through in-situ x-ray scanning, and the those calculated at the two corresponding strain levels using both the solid and beam models. Although this is a qualitative comparison, the figure shows that both models can well capture the deformation patterns of the open cell foam under compression as exhibited by the actual CT reconstructed geometry. Bending of the struts takes place, with isolated local buckling phenomena due to the foam compression. Compared to the solid model, Von Mises stresses for the beam model are slightly higher, although within the same range. The deformation of several struts of the beam model is more severe than that of the solid model. The difference might derive from the size and shape of the simulated struts joint area: the stiffness of this area has a higher stiffness than that of the struts connected to it, which has a direct influence on the deformation of the struts. The distribution of stresses on the struts allows for a richer description of the stress concentration compared to the beam model, in which the distribution of stress on the strut is more uniform, unable to extract local stress–strain characteristics. Yet, based on the global response presented in Fig. 27, it would seem that these local effects have a very limited impact on the overall behavior.

The introduction of local defects (e.g. surface roughness), strut profile parameters (shape, curvature) and other morphological features could be considered to improve the current capabilities of the beam model, but these options should be carefully weighed against the inevitable increase of the required computational costs.

7.3. *Computational cost*

For the 10 mm x 10 mm x10mm model, the number of elements, memory allocations and CPU time used for simulation under same conditions are shown in Table 3, with reference to a cluster node equipped with 2 Dell Power Edge R410 nodes with Intel(R) Xeon(R) CPU X5650 @ 2.67 GHz, 24 cores, 48 GB RAM. Compared to the solid model, the beam model demonstrates extremely efficient computing capabilities. The memory allocated for beam model during simulation is about one fifteenth of that allocated to the solid model. This greatly improves computing efficiency while reducing hardware requirements. The running time for the beam models is also shorter than that of the solid model by a factor 20, i.e. 4 h instead of 3 days.

8. Conclusions

Due to the unique internal connectivity and three-dimensional skeleton structure, polymeric open cell foam structures have a wide range of properties and are suitable for many applications. Based on the images obtained by CT scan, the morphological features of the foam microstructure were used to generate a simplified finite element model. This variable cross-section beam model exhibits high consistency with the realistic microstructure of the foam. This improved image-based finite element modelling method increases the computational efficiency of the simulation and could serve as an advanced means to investigate the mechanical performance of the foam under compression. The main conclusions of this research are as follows:

1. The images of the PU PPI20 open cell foam microstructure were obtained by CT scan. The 3D solid model of the microstructure was converted from these images using Level-set method and Delaunay triangulation. The morphological features (strut length and thickness) were then extracted.

2 A variable cross-section beam model was created based on the measured morphological features. The simulations using the solid model and beam model were carried out. The comparison between the simulation results and the experimental results proved the effectiveness of this simplified image-based modelling method. The beam model demonstrates high computational efficiency compared to the solid model which could contribute to the fast and accurate design of the new foam structures.

The influence of morphological features such as the shape of the strut and the joint area approximation on the modelling accuracy still needs to be investigated in the future. The beam model, however, already proves a valuable tool to optimize the design of open cell foam products. Thanks to its computational efficiency, relatively large models can be built while retaining essential information about the true foam morphology. Additionally, the model could be exploited to generate a very large number of foam architectures and investigate the correlation between key morphological parameters and the overall mechanical behavior, in view of identifying suitable homogenized models whose constitutive parameters can be objectively determined for a given foam structure and constituent material.

Although the model has been defined on the basis of images and results of in-situ mechanical tests of a specific case, it abstracts the general characteristics of this type of foam and can therefore be used to predict the behavior under different loading conditions, such as may arise in typical applications of these materials. The proposed approach is not limited to polymeric foams but can be readily extended to other materials (e.g. trabecular bone), provided they possess an open cell structure. For closed cell foams, the model will require further development with the inclusion of additional elements coupled to the beam network (e.g. shell elements).

CRediT authorship contribution statement

Shaoheng Feng: Writing – review & editing, Writing – original draft, Visualization, Validation, Methodology, Investigation, Formal analysis, Data curation, Conceptualization. **Luca Andena:** Writing – review & editing, Supervision, Resources, Project administration, Methodology, Funding acquisition, Conceptualization. **Michele Nacucchi:** Software, Resources, Methodology, Investigation, Data curation. **Fabio De Pascalis:** Software, Resources, Methodology, Investigation, Data curation.

Declaration of competing interest

The authors declare that they have no known competing financial interests or personal relationships that could have appeared to influence the work reported in this paper.

Acknowledgments

Shaoheng Feng gratefully acknowledges financial support from China Scholarship Council (Grant No. 202108070140). The authors also wish to thank Dr. Marco Contino and Mr. Oscar Bressan for their support in carrying out experimental activities.

Appendix

Figs. A1-A5 report the results of preliminary parametric analyses which helped the definition of the model presented in the paper by investigating the influence of:

- Constitutive material law for the PU foam
- Value of the Poisson’s ratio coefficient
- Beam element size
- Value of the coefficient of friction between PU foam and steel platen
- Mechanical anisotropy analysis using experiments and simulations

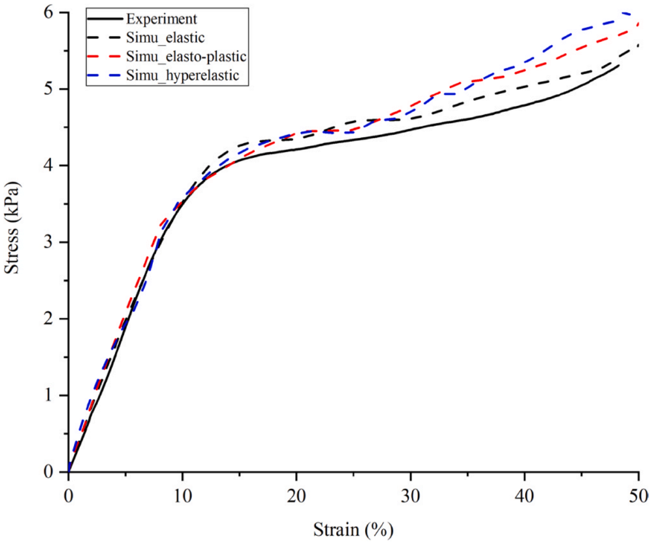

Fig. A1. The comparison of experimental results and simulation results using different constitutive laws

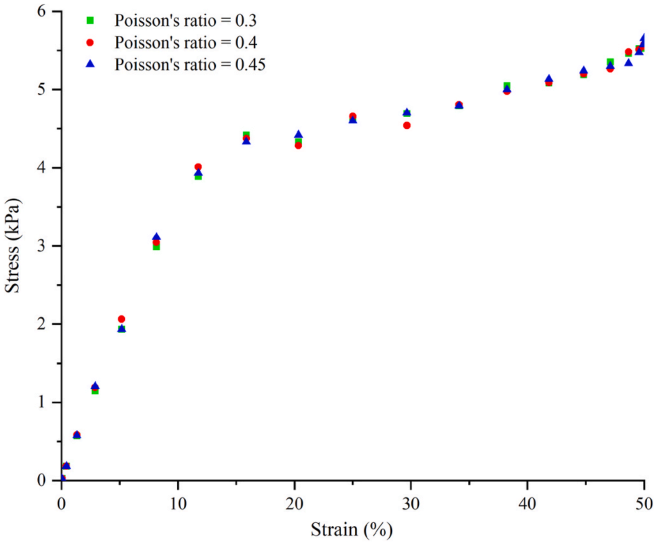

Fig. A2. The effect of Poisson’s ratio on the simulation using solid model

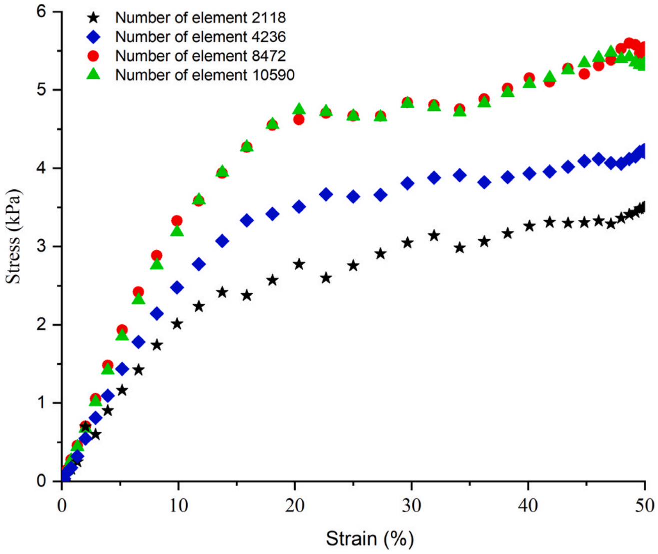

Fig. A3. Beam model mesh sensitivity analysis

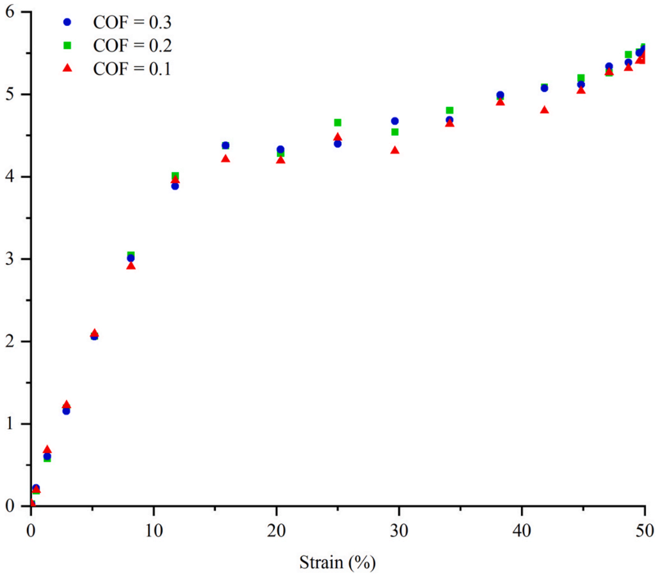

Fig. A4. The effect of coefficient of friction on the simulation using solid model

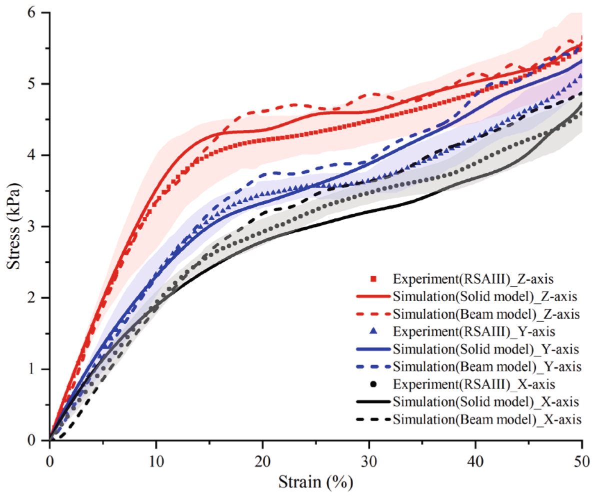

(a) Nominal stress-strain curves along different directions derived from experiments (RSAIII) and simulations (solid model and beam model)

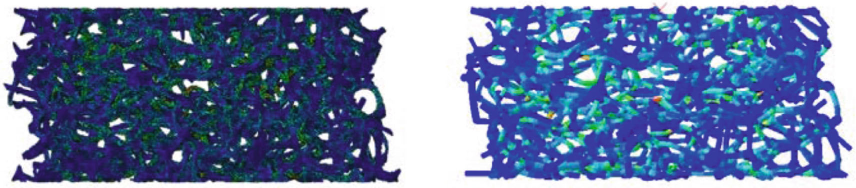

(b) Deformation at 50% strain along X-axis. Solid model (Left) and Beam model (Right)

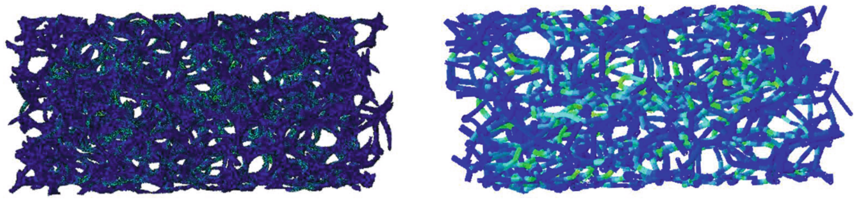

(c) Deformation at 50% strain along Y-axis. Solid model (Left) and Beam model (Right)

Fig. A5. Mechanical anisotropy of PU PPI20 foam

Data availability

Data will be made available on request.

References

Jacobs, L.J., Kemmere, M.F., Keurentjes, J.T., 2008. Sustainable polymer foaming using high pressure carbon dioxide: a review on fundamentals, processes and applications. Green Chem. 10, 731–738. https://doi.org/10.1039/B801895B.

Amir, N., Hisham, M. S. M., Abidin, K. A. Z., 2018. Study of physical properties and shock absorption abilities of starch polymer foam as cushioning material for packaging. In: MATEC Web of Conferences. EDP Sciences, Vol. 225, pp. 06010. doi: 10.1051/matecconf/201822506010.

de Souza, F. M., Choi, J., Ingsel, T., Gupta, R. K., 2022. High-performance polyurethanes foams for automobile industry. In: Nanotechnology in the Automotive Industry. Elsevier, pp. 105-129. doi: 10.1016/B978-0-323-90524-4.00006-2.

Matzke, E.B., 1945. The three-dimensional shapes of bubbles in foams. Proc. Natl. Acad. Sci. U.S. A. 31 (9), 281–289. https://doi.org/10.1073/pnas.31.9.281.

Matzke, E.B., 1946. The three-dimensional shape of bubbles in foam-an analysis of the role of surface forces in three-dimensional cell shape determination. Am. J. Bot. 58–80. https://doi.org/10.2307/2437492.

Kraynik, A.M., Reinelt, D.A., van Swol, F., 2003. Structure of random monodisperse foam. Phys. Rev. E. 67 (3), 031403. https://doi.org/10.1103/PhysRevE.67.031403.

Kraynik, A.M., 2003. Foam structure: From soap froth to solid foams. MRS Bull. 28 (4), 275–278. https://doi.org/10.1557/mrs2003.80.

Kraynik, A.M., Reinelt, D.A., van Swol, F., 2004. Structure of random foam. Phys. Rev. Lett. 93 (20), 208301. https://doi.org/10.1103/PhysRevLett.93.208301.

Gent, A.N., Thomas, A.G., 1959. The deformation of foamed elastic materials. J. Appl. Polym. Sci. 1 (1), 107–113. https://doi.org/10.1002/app.1959.070010117.

Lederman, J.M., 1971. The prediction of the tensile properties of flexible foams. J. Appl. Polym. Sci. 15 (3), 693–703. https://doi.org/10.1002/app.1971.070150314.

Gibson, I.J., Ashby, M.F., 1982. The mechanics of three-dimensional cellular materials. Proc. R. Soc. Lond. A Math Phys Sci. 382 (1782), 43–59. https://doi.org/10.1098/rspa.1982.0088.

Zhu, H.X., Knott, J.F., Mills, N.J., 1997. Analysis of the elastic properties of open-cell foams with tetrakaidecahedral cells. J. Mech. Phys. Solids. 45 (3), 319–343. https://doi.org/10.1016/S0022-5096(96)00090-7.

Warren, W.E., Kraynik, A.M., 1997. Linear elastic behavior of a low-density Kelvin foam with open cells. J. Appl. Mech. 64 (4), 787–794. https://doi.org/10.1115/1.2788983.

Li, K., Gao, X.L., Roy, A.K., 2003. Micromechanics model for three-dimensional open-cell foams using a tetrakaidecahedral unit cell and Castigliano's second theorem.

Compos. Sci. Technol. 63 (12), 1769–1781. https://doi.org/10.1016/S0266-3538(03)00117-9.

Warren, W.E., Kraynik, A.M., 1988. The linear elastic properties of open-cell foams. J. Appl. Mech. 55 (2), 341–346. https://doi.org/10.1115/1.3173680.

Ghosh, I., 2009. Heat transfer correlation for high-porosity open-cell foam. Int. J. Heat Mass Transf. 52 (5–6), 1488–1494. https://doi.org/10.1016/j.ijheatmasstransfer.2008.07.047.

Klumpp, M., Inayat, A., Schwerdtfeger, J., Körner, C., Singer, R.F., Freund, H., Schwieger, W., 2014. Periodic open cellular structures with ideal cubic cell geometry: Effect of porosity and cell orientation on pressure drop behavior. J. Chem. Eng. 242, 364–378. https://doi.org/10.1016/j.cej.2013.12.060.

Buffel, B., Desplentere, F., Bracke, K., Verpoest, I., 2014. Modelling open cell-foams based on the Weaire–Phelan unit cell with a minimal surface energy approach. Int. J. Solids Struct. 51 (19–20), 3461–3470. https://doi.org/10.1016/j.ijsolstr.2014.06.017.

Mills, N.J., 2007. The high strain mechanical response of the wet Kelvin model for open-cell foams. Int. J. Solids Struct. 44 (1), 51–65. https://doi.org/10.1016/j.ijsolstr.2006.04.014.

Jang, W.Y., Kraynik, A.M., Kyriakides, S., 2008. On the microstructure of open-cell foams and its effect on elastic properties. Int. J. Solids Struct. 45 (7–8), 1845–1875. https://doi.org/10.1016/j.ijsolstr.2007.10.008.

Jang, W.Y., Kyriakides, S., Kraynik, A.M., 2010. On the compressive strength of open-cell metal foams with Kelvin and random cell structures. Int. J. Solids Struct. 47 (21), 2872–2883. https://doi.org/10.1016/j.ijsolstr.2010.06.014.

Kaoua, S.A., Boutaleb, S., Dahmoun, D., Azzaz, M., 2016. Numerical modelling of open-cell metal foam with Kelvin cell. Comput. Appl. Math. 35, 977–985. https://doi.org/10.1007/s40314-015-0217-4.

Song, Y., Wang, Z., Zhao, L., Luo, J., 2010. Dynamic crushing behavior of 3D closed-cell foams based on Voronoi random model. Mater. Des. 31 (9), 4281–4289. https://doi.org/10.1016/j.matdes.2010.04.007.

Martínez, J., Dumas, J., Lefebvre, S., 2016. Procedural voronoi foams for additive manufacturing. ACM Trans. Graph. 35 (4), 1–12. https://doi.org/10.1145/2897824.2925922.

Wang, S., Ding, Y., Yu, F., Zheng, Z., Wang, Y., 2020. Crushing behavior and deformation mechanism of additively manufactured Voronoi-based random open-cell polymer foams. Mater. Today Commun. 25, 101406. https://doi.org/10.1016/j.mtcomm.2020.101406.

Inayat, A., Schwerdtfeger, J., Freund, H., Körner, C., Singer, R.F., Schwieger, W., 2011. Periodic open-cell foams: Pressure drop measurements and modeling of an ideal tetrakaidecahedra packing. Chem. Eng. Sci. 66 (12), 2758–2763. https://doi.org/10.1016/j.ces.2011.03.031.

De Jaeger, P., T'Joen, C., Huisseune, H., Ameel, B., De Paepe, M., 2011. An experimentally validated and parameterized periodic unit-cell reconstruction of open-cell foams. J. Appl. Phys. 109 (10). https://doi.org/10.1063/1.3587159.

Ramírez, J.F., Cardona, M., Velez, J.A., Mariaka, I., Isaza, J.A., Mendoza, E., Fernández-Morales, P., 2014. Numerical modeling and simulation of uniaxial compression of aluminum foams using FEM and 3D-CT images. Procedia Mater. Sci. 4, 227–231. https://doi.org/10.1016/j.mspro.2014.07.609.

Tagliabue, S., Andena, L., Nacucchi, M., De Pascalis, F., 2021. An image-based approach for structure investigation and 3D numerical modelling of polymeric foams. J. Polym. Res. 28 (3), 75. https://doi.org/10.1007/s10965-021-02438-9.

Belda, R., Palomar, M., Marco, M., Vercher-Martínez, A., Giner, E., 2021. Open cell polyurethane foam compression failure characterization and its relationship to morphometry. Mater. Sci. Eng. C 120, 111754. https://doi.org/10.1016/j.msec.2020.111754.

Daphalapurkar, N.P., Hanan, J.C., Phelps, N.B., Bale, H., Lu, H., 2008. Tomography and simulation of microstructure evolution of a closed-cell polymer foam in compression. Mech. Adv. Mater. Struct. 15 (8), 594–611. https://doi.org/10.1080/15376490802470523.

Sun, Y., Li, Q.M., Lowe, T., McDonald, S.A., Withers, P.J., 2016. Investigation of strain-rate effect on the compressive behaviour of closed-cell aluminium foam by 3D image-based modelling. Mater. Des. 89, 215–224. https://doi.org/10.1016/j.matdes.2015.09.109.

Bhagavathula, K.B., Meredith, C.S., Ouellet, S., Satapathy, S.S., Romanyk, D.L., Hogan, J.D., 2022. Density, microstructure, and strain-rate effects on the compressive response of polyurethane foams. Exp. Mech. 1–15. https://doi.org/10.1007/s11340-021-00772-z.

Jang, W.Y., Kyriakides, S., 2009. On the crushing of aluminum open-cell foams: Part I. Experiments. Int. J. Solids Struct. 46 (3–4), 617–634. https://doi.org/10.1016/j.ijsolstr.2008.09.008.

Singh, R., Lee, P.D., Lindley, T.C., Kohlhauser, C., Hellmich, C., Bram, M., Imwinkelried, T., Dashwood, R.J., 2010. Characterization of the deformation behavior of intermediate porosity interconnected Ti foams using micro-computed tomography and direct finite element modeling. Acta Biomater. 6 (6), 2342–2351. https://doi.org/10.1016/j.actbio.2009.11.032.

Adrien, J., Maire, E., Gimenez, N., Sauvant-Moynot, V., 2007. Experimental study of the compression behaviour of syntactic foams by in situ X-ray tomography. Acta Mater. 55 (5), 1667–1679. https://doi.org/10.1016/j.actamat.2006.10.027.

Elliott, J.A., Windle, A.H., Hobdell, J.R., Eeckhaut, G., Oldman, R.J., Ludwig, W., Boller, E., Cloetens, P., Baruchel, J., 2002. In-situ deformation of an open-cell flexible polyurethane foam characterised by 3D computed microtomography. J. Mater. Sci. 37, 1547–1555. https://doi.org/10.1023/A:1014920902712.

Gong, L., Kyriakides, S., Jang, W.Y., 2005. Compressive response of open-cell foams. Part I: Morphology and elastic properties. Int. J. Solids Struct. 42 (5–6), 1355–1379. https://doi.org/10.1016/j.ijsolstr.2004.07.023.

Gaitanaros, S., Kyriakides, S., Kraynik, A.M., 2012. On the crushing response of random open-cell foams. Int. J. Solids Struct. 49 (19–20), 2733–2743. https://doi.org/10.1016/j.ijsolstr.2012.03.003.

Tran, L.V., Niiranen, J., 2020. A geometrically nonlinear Euler–Bernoulli beam model within strain gradient elasticity with isogeometric analysis and lattice structure applications. Math. Mech. Complex Syst. 8 (4), 345–371. https://doi.org/10.2140/memocs.2020.8.345.

Liu, F., Wang, L., Jin, D., Liu, X., Lu, P., 2021. Equivalent beam model for spatial repetitive lattice structures with hysteretic nonlinear joints. Int. J. Mech. Sci. 200, 106449. https://doi.org/10.1016/j.ijmecsci.2021.106449.

Weeger, O., Valizadeh, I., Mistry, Y., Bhate, D., 2023. Inelastic finite deformation beam modeling, simulation, and validation of additively manufactured lattice structures. Addit. Manuf. Lett. 4, 100111. https://doi.org/10.1016/j.addlet.2022.100111.

Zhou, X., Yang, J., Shen, L., Xie, X., Tang, J., Zhao, G., Xu, J., 2024. A new modelling method for open cell foam structure based on centroidal and capacity constraint power diagram. J. Sandw. Struct. Mater. 26 (5), 662–678. https://doi.org/10.1177/10996362231226334.

Luxner, M.H., Stampfl, J., Pettermann, H.E., 2005. Finite element modeling concepts and linear analyses of 3D regular open cell structures. J. Mater. Sci. 40, 5859–5866. https://doi.org/10.1007/s10853-005-5020-y.

Große, J., Dietrich, B., Martin, H., Kind, M., Vicente, J., Hardy, E.H., 2008. Volume image analysis of ceramic sponges. Chem. Eng. Technol. 31 (2), 307–314. https://doi.org/10.1002/ceat.200700403.

Labeas, G.N., Sunaric, M.M., 2010. Investigation on the static response and failure process of metallic open lattice cellular structures. Strain 46 (2), 195–204. https://doi.org/10.1111/j.1475-1305.2008.00498.x.

Smith, M., Guan, Z.W., Cantwell, W.J., 2013. Finite element modelling of the compressive response of lattice structures manufactured using the selective laser melting technique. Int. J. Mech. Sci. 67, 28–41. https://doi.org/10.1016/j.ijmecsci.2012.12.004.

Elmoutaouakkil, A., Fuchs, G., Bergounhon, P., Peres, R., Peyrin, F., 2003. Three-dimensional quantitative analysis of polymer foams from synchrotron radiation x-ray microtomography. J. Phys. D Appl. Phys. 36 (10A), A37. https://doi.org/10.1088/0022-3727/36/10A/308.

Pérez-Tamarit, S., Solórzano, E., Hilger, A., Manke, I., Rodríguez-Pérez, M.A., 2018. Multi-scale tomographic analysis of polymeric foams: A detailed study of the cellular structure. Eur. Polym. J. 109, 169–178. https://doi.org/10.1016/j.eurpolymj.2018.09.047.

Kirchner, M., Fridrich, J., 2010. On detection of median filtering in digital images. Media forensics and security II, SPIE 7541, 371–382. https://doi.org/10.1117/12.839100.

Li, C., Xu, C., Gui, C., Fox, M.D., 2010. Distance regularized level set evolution and its application to image segmentation. IEEE Trans. Image Process. 19 (12), 3243–3254. https://doi.org/10.1109/TIP.2010.2069690.

Teran, J., Molino, N., Fedkiw, R., Bridson, R., 2005. Adaptive physics based tetrahedral mesh generation using level sets. Eng. Comput. 21, 2–18. https://doi.org/10.1007/s00366-005-0308-8.

Li, H., Yamada, T., Jolivet, P., Furuta, K., Kondoh, T., Izui, K., Nishiwaki, S., 2021. Full-scale 3D structural topology optimization using adaptive mesh refinement based on the level-set method. Finite Elem. Anal. Des. 194, 103561. https://doi.org/10.1016/j.finel.2021.103561.

Rebay, S., 1993. Efficient unstructured mesh generation by means of Delaunay triangulation and Bowyer-Watson algorithm. J. Comput. Phys. 106 (1), 125–138. https://doi.org/10.1006/jcph.1993.1097.

Yan, Y., Sykes, K., Chambers, E., Letscher, D., Ju, T., 2016. Erosion thickness on medial axes of 3D shapes. ACM Trans Graph. 35 (4), 1–12. https://doi.org/10.1145/2897824.2925938.

Danielsson, P.E., 1980. Euclidean distance mapping. Comput. Graph. Image Process. 14 (3), 227–248. https://doi.org/10.1016/0146-664X(80)90054-4.

Kumar, P., Topin, F., 2014. Micro-structural impact of different strut shapes and porosity on hydraulic properties of Kelvin-like metal foams. Transp. Porous Media. 105, 57–81. https://doi.org/10.1007/s11242-014-0358-8.

Kumar, P., Topin, F., Tadrist, L., 2015. Geometrical characterization of Kelvin-like metal foams for different strut shapes and porosity. J. Porous Media. 18 (6). https://doi.org/10.1615/JPorMedia.v18.i6.70.

Plateau, J.A.F., 1873. Statique expérimentale et théorique des liquides soumis aux seules forces moléculaires. Vol. 2, Gauthier-Villars. https://hdl.handle.net/2268/332053.

Astm d6226–21,, 2021. Standard Test Method for Open Cell Content of Rigid Cellular Plastics. ASTM International, Annual Book of ASTM Standards.

Shafarenko, L., Petrou, M., Kittler, J., 1997. Automatic watershed segmentation of randomly textured color images. IEEE Trans. Image Process. 6 (11), 1530–1544. https://doi.org/10.1109/83.641413.

Harrigan, T.P., Mann, R.W., 1984. Characterization of microstructural anisotropy in orthotropic materials using a second rank tensor. J. Mater. Sci. 19, 761–767. https://doi.org/10.1007/BF00540446.

Ketcham, R.A., Ryan, T.M., 2004. Quantification and visualization of anisotropy in trabecular bone. J. Microsc. 213 (2), 158–171. https://doi.org/10.1111/j.1365-2818.2004.01277.x.

Dong, G., Zhao, Y.F., 2018. Numerical and experimental investigation of the joint stiffness in lattice structures fabricated by additive manufacturing. Int. J. Mech. Sci. 148, 475–485. https://doi.org/10.1016/j.ijmecsci.2018.09.014.

Park, S.I., Rosen, D.W., 2018. Homogenization of mechanical properties for material extrusion periodic lattice structures considering joint stiffening effects. J. Mech. Des. 140 (11), 111414. https://doi.org/10.1115/1.4040704.

ASTM D1621-16, 2023. Standard Test Method for Compressive Properties of Rigid Cellular Plastics. ASTM International, Annual Book of ASTM Standards.

ASTM D638-14, 2022. Standard Test Method for Tensile Properties of Plastics. ASTM International, Annual Book of ASTM Standards.

Gong, L., Kyriakides, S., 2005. Compressive response of open cell foams Part II: Initiation and evolution of crushing. Int. J. Solids Struct. 42 (5–6), 1381–1399. https://doi.org/10.1016/j.ijsolstr.2004.07.024.

Zhu, H.X., Windle, A.H., 2002. Effects of cell irregularity on the high strain compression of open-cell foams. Acta Mater. 50 (5), 1041–1052. https://doi.org/10.1016/S1359-6454(01)00402-5.

Kanakkanatt, S.V., 1973. Mechanical anisotropy of open-cell foams. J. Cell. Plast. 9 (1), 50–53. https://doi.org/10.1177/0021955X7300900109.

Huber, A.T., Gibson, L.J., 1988. Anisotropy of foams. J. Mater. Sci. 23 (8), 3031–3040. https://doi.org/10.1007/BF00547486.